



**HAL**  
open science

## Monitoring and reactive-transport modeling of the spatial and temporal variations of the Strengbach spring hydrochemistry

Julien Ackerer, François Chabaux, Yann Lucas, Alain Clément, Bertrand Fritz, Emilie Beaulieu, Daniel Viville, Pierret Mc, Sophie Gangloff, Philippe Négrel

### ► To cite this version:

Julien Ackerer, François Chabaux, Yann Lucas, Alain Clément, Bertrand Fritz, et al.. Monitoring and reactive-transport modeling of the spatial and temporal variations of the Strengbach spring hydrochemistry. *Geochimica et Cosmochimica Acta*, 2018, 225, pp.17-35. 10.1016/j.gca.2018.01.025 . hal-03885578

**HAL Id: hal-03885578**

**<https://hal.science/hal-03885578>**

Submitted on 5 Dec 2022

**HAL** is a multi-disciplinary open access archive for the deposit and dissemination of scientific research documents, whether they are published or not. The documents may come from teaching and research institutions in France or abroad, or from public or private research centers.

L'archive ouverte pluridisciplinaire **HAL**, est destinée au dépôt et à la diffusion de documents scientifiques de niveau recherche, publiés ou non, émanant des établissements d'enseignement et de recherche français ou étrangers, des laboratoires publics ou privés.

1                                   **Monitoring and reactive-transport modeling of the spatial**  
2                                   **and temporal variations of the Strengbach spring hydrochemistry**  
3

4  
5   Ackerer J.<sup>1</sup>, Chabaux F.<sup>1</sup>, Lucas Y.<sup>1</sup>, Clément A.<sup>1</sup>, Fritz B.<sup>1</sup>, Beaulieu E.<sup>1</sup>, Viville D.<sup>1</sup>, Pierret MC<sup>1</sup>,  
6                                   Gangloff S.<sup>1</sup>, Négrel Ph.<sup>2</sup>

7           (1) Laboratoire d'Hydrologie et de Géochimie de Strasbourg (UMR 7517), CNRS,  
8                                   Université de Strasbourg, 1 rue Blessig, 67084 Strasbourg cedex, France.

9           (2) Bureau de Recherches Géologiques et Minières (BRGM), 3 Avenue Claude Guillemin,  
10                                  45000 Orléans, France.

11  
12  
13  
14  
15  
16  
17  
18  
19  
20  
21  
22  
23  
24  
25  
26  
27  
28  
29

30 **Abstract:**

31 This study focuses on 20 years of hydrochemical monitoring of the small springs that emerge  
32 in the experimental granitic catchment of Strengbach (OHGE, France) and the simulation of  
33 these data using the KIRMAT code. The data indicate that the Strengbach springs display  
34 chemostatic behavior; that is, limited temporal variations were noted in the concentrations  
35 of dissolved silica ( $\text{H}_4\text{SiO}_4$ ) and most of the basic cations during the studied period (1987-  
36 2010), resulting in relative stability of the global weathering fluxes exported by the springs.  
37 Only the  $\text{Ca}^{2+}$  concentrations reflect a significant decrease in all the Strengbach springs since  
38 1987, and the variations differ from one spring to another. The modeling results show that  
39 the decrease in  $\text{Ca}^{2+}$  in the Strengbach springs is due to the response of the water-rock  
40 interactions within the bedrock to the variations in the chemical composition of the soil  
41 solutions, which were characterized by a significant increase in pH and a decrease in  $\text{Ca}^{2+}$   
42 concentrations between 1987 and 2010. The decrease in  $\text{Ca}^{2+}$  concentrations seen in the  
43 Strengbach springs is controlled by changes in the apatite dissolution rate and the  
44 compositions of clay minerals induced by the soil solution changes. The differences observed  
45 between the  $\text{Ca}^{2+}$  trends of the springs are related to changes in the residence time of the  
46 water supplying the different springs. The weak impact of the soil solution modifications on  
47 the dissolution rates of other primary minerals and on the bulk precipitation rates of the clay  
48 minerals explains the relative stability over time of the concentrations of the other cations  
49 and dissolved silica in the water derived from the Strengbach springs. Further, the  
50 hydrochemical simulations suggest that the chemostatic behavior of the Strengbach springs  
51 cannot be explained by the mobilization of waters that are close to chemical equilibrium.  
52 Finally, a comparison of current and long-term weathering rates determined from the spring  
53 water monitoring and a regolith profile shows that the modern chemical fluxes of  $\text{Ca}^{2+}$  are  
54 higher than the long-term ones, whereas the weathering fluxes of  $\text{H}_4\text{SiO}_4$  and  $\text{Na}^+$  have likely  
55 been much more stable over time. All of these results indicate that the silicate weathering  
56 processes are characterized by weak spatial and temporal variability in the Strengbach  
57 catchment, while the chemical elements such as  $\text{Ca}^{2+}$ , for which the budget in the spring  
58 waters is controlled by the dynamic behavior of clay minerals and minor minerals, are  
59 significantly affected by Quaternary climatic variations and decennial environmental  
60 changes.

61

62 **Keywords:** long-term hydrochemical monitoring, weathering fluxes, reactive-transport  
63 modeling, Water-rock interactions, critical zone observatory.

64

65

## 66 **1-Introduction**

67

68 Continental silicate weathering is one of the major factors that controls the chemical  
69 evolution of the Earth's surface. From the large-scale transport of solutes by rivers to the  
70 development of regolith on hillslopes, complex relationships and linkages exist between  
71 weathering, erosion, vegetation and climate (Egli et al., 2008; Godd ris et al., 2009; Beaulieu  
72 et al., 2012; Donnini et al., 2016). Numerical approaches and reactive transport models have  
73 become a powerful tool to explore the forces that drive chemical weathering on scales  
74 ranging from small watersheds to continentals (Beaulieu et al., 2010; Lebedeva et al., 2010;  
75 Godd ris and Brantley, 2013; Li et al., 2014; Schaffhauser et al., 2014). The aim of this study  
76 is to illustrate the potential of the hydrochemical approaches at the scale of an elementary  
77 watershed, the Strengbach watershed in France. The Strengbach catchment is one of the  
78 reference sites for the critical zone observatories in France ("Observatoire  
79 Hydrog ochimique de l'Environnement", OHGE, <http://ohge.unistra.fr>; <http://rnbv.ipgp.fr>).  
80 This experimental catchment is one of the few critical zone observatories in the world where  
81 geochemical data on soil solutions, streams, and springs have been collected for 20 years;  
82 moreover, mineralogical characterization of the soils and bedrock has been carried out. It is  
83 a relevant site where hydrochemical modeling approaches can be applied to study the origin  
84 of spatial and temporal variations in the chemical composition of surface waters. The results  
85 obtained in this study highlight the interest of this approach in improving our understanding  
86 of the main processes controlling the chemical variability of surface waters and providing  
87 insights into the sensitivity of weathering processes to recent environmental changes and to  
88 Quaternary climatic variations.

89

90

## 91 **2-Site description**

92

93 The Strengbach catchment is a small watershed (0.8 km<sup>2</sup>), where multidisciplinary studies  
94 have been carried out since 1986 (“Observatoire Hydrogéochimique de l’Environnement”,  
95 OHGE). It is located in the Vosges Mountains of northeastern France (Figure 1) at altitudes  
96 between 883 and 1147 m a.s.l. The current climate is mountainous oceanic. The annual  
97 mean temperature is 6 °C, the annual mean rainfall is 1400 mm, the annual mean runoff is  
98 about 800 mm, and the annual mean evapotranspiration has been estimated to be about  
99 600 mm (Viville et al., 2012). Snowfall occurs from December to March and the major  
100 hydrological and high-flow events frequently occur during snowmelt periods at the end of  
101 the winter season. A saturated area is situated close to the watershed outlet and is  
102 connected to the Strengbach stream. The soils of the watershed, which range from  
103 Hyperdystric Cambisols to Entic Podzols (WRB, 2006), are acidic, coarse in texture, and are  
104 less than 1 m in thickness. A mixed forest composed of beech and spruce covers up to 90%  
105 of the catchment. During the 1980s, the watershed experienced acid atmospheric  
106 deposition, and scientific investigations have been conducted to understand the observed  
107 tree mortality and the needle yellowing of the spruce stands (Probst et al, 1990; Dambrine et  
108 al., 1998). The bedrock is a coarse-grained Hercynian granite that has been affected by  
109 hydrothermal events and is characterized by low contents of base cations, especially Ca  
110 (Fichter et al., 1998). The granite is strongly hydrothermally altered within the northern part  
111 of the watershed, and it is relatively weakly affected by hydrothermal processes on the  
112 southern slopes. The hydrothermal events caused a decrease in the abundances of K-  
113 feldspar and albite in the granite and promoted the precipitation of quartz, hematite and

114 fine-grained white mica in veins (El Gh'Mari, 1995). Several small but permanent springs  
115 emerge on both hillsides of the catchment (Figure 1).

### 116 **3-Sample location and data acquisition**

117 This study is based on the data obtained from the hydrochemical monitoring carried out in  
118 the Strengbach experimental catchment. More specifically, it focuses on comparing the  
119 chemical compositions of several springs emerging in the Strengbach watershed and  
120 understanding their geochemical variations during the period between 1990 and 2010. Four  
121 springs, the CS springs (Figure 1), are located within the southern part of the Strengbach  
122 catchment, where the bedrock is weakly affected by hydrothermal alteration. Each spring  
123 sources is a fracture in the granitic bedrock at a depth of 2 to 5 m. These four springs then  
124 gather in a single collector (CR). The water that accumulates in this collector is used to  
125 supply drinking water to the neighboring village of Aubure. The two other springs (RH3 and  
126 ARG) used in this study emerge naturally on the slopes. The RH3 spring is located on the  
127 hydrothermally altered northern part of the watershed. The other natural spring, the ARG  
128 spring, also lies within the northern part of the watershed, but it occurs near the Strengbach  
129 stream (Figure 1). A detailed study of the geochemical variations in the spring and stream  
130 waters of the Strengbach watershed can be found in Prunier, (2008) and in Pierret et al.  
131 (2014) for the period 2004-2006. These studies analyzed major and trace element  
132 concentrations,  $^{87}\text{Sr}/^{86}\text{Sr}$  isotope ratios, and the ( $^{234}\text{U}/^{238}\text{U}$ ) activity ratios of the waters. The  
133 results suggested that each spring is characterized by a rather stable and independent water  
134 pathway within the watershed substratum (Pierret et al., 2014), as was also proposed for a  
135 neighboring granitic watershed in the Vosges Mountains, the Ringelbach watershed  
136 (Schaffhauser et al., 2014). Soil solutions have been sampled from 1992 to 2010 at two

137 different locations (Figure 1), one at a beech site on the southern slope (the beech stand is  
138 locally named HP) and one at a spruce site on the northern slope (the spruce stand is named  
139 VP; the data are given in Prunier et al., 2015). All water samples, which represent spring  
140 waters, soil solutions and rainwater, were filtered soon after collection with 0.45- $\mu\text{m}$   
141 cellulose acetate membrane filters, stored in cleaned polyethylene bottles and conserved in  
142 a cold room until they were analyzed chemically. The analysis of water chemistry was  
143 performed by following techniques used at LHyGeS (Strasbourg, France), described by Probst  
144 et al. (1990) and Dambrine et al. (1998; for the 1986-1998 period) and by Gangloff et al.  
145 (2014; for the samples collected after 2000). In addition, the mineralogical compositions and  
146 the petrological properties of two rocks that are representative of the two extreme granitic  
147 facies constituting the bedrock of the watershed have been assessed. These rocks include a  
148 sample of strongly hydrothermally altered granite, the CA sample, which was collected in the  
149 northern part of the watershed, and a granitic sample from the southern slope, the HPT  
150 sample, which is weakly affected by hydrothermal processes (Figure 1). Mineralogical and  
151 petrological data on these two samples can be found in El Gh'Mari (1995) and are  
152 summarized in Table 1. Discharges of water from the springs were also measured regularly.  
153 Together with the major element concentrations, these data enable estimation of the  
154 dissolved fluxes exported by each spring.

#### 155 **4-Spatial variability and temporal evolution of the spring water chemistry**

##### 156 **4-1-Spatial and seasonal variability**

157 The geochemical data obtained from the different springs confirm the occurrence of spatial  
158 variations of spring water chemistry at the watershed scale, especially between the northern  
159 part of the watershed, which is strongly hydrothermally altered, and the southern slopes,



160 which are weakly affected by hydrothermal processes. Such variations were highlighted by  
161 Pierret et al. (2014) and in Prunier (2008), in that the elemental ratios (i.e., Mg/Na Ca/Na,  
162 and K/Na) and Sr isotopic ratios show different values between the two slopes of the  
163 watershed. Mg<sup>2+</sup> differs most strongly between the two slopes, and systematically higher  
164 values of this species were noted in the RH3 spring than in the CS springs (Figure 2a). This  
165 difference is likely related to the higher Mg content in the hydrothermally altered granite  
166 facies, and the presence of gneiss may influence the chemical composition of the source  
167 waters in the northern part of the catchment (Fichter et al., 1998; Pierret et al., 2014).  
168 Slightly higher concentrations of K<sup>+</sup> and to a lesser extent Ca<sup>2+</sup> occur in the RH3 spring, which  
169 drains the northern part of the catchment. The concentrations of the other species, such as  
170 H<sub>4</sub>SiO<sub>4</sub>, Na<sup>+</sup>, and the anions, as well as pH and alkalinity, show some slight differences from  
171 one spring to another, with no systematic differences identified between the two hillslopes.  
172 For a given spring at the annual timescale, the data indicate relative stability of the silica and  
173 cation concentrations under widely varying discharges. Solute concentrations vary in the  
174 spring waters by less than 15 %, whereas discharge can vary by more than a factor of 10,  
175 implying that concentrations are relatively stable over a wide range of hydrological  
176 conditions, and that seasonal fluctuations are relatively limited.

#### 177 **4-2-Long-term inter-annual variability**

178 At the inter-annual timescale, the 20 years of chemical monitoring data reflect systematic  
179 trends in the chemical concentrations with time, but not all chemical species are affected, as  
180 is well demonstrated by the water samples obtained from the CR collector (Figure 3).  
181 Magnitudes of these long-term concentration variations can be different from one spring to  
182 another (Figure 4, in Electronic Annex Figure EA1). Species that show the most significant

183 long-term changes in concentrations, with amplitudes much higher than the seasonal  
184 fluctuations, include  $\text{Ca}^{2+}$  (Figure 2b) and (to a lesser extent)  $\text{Mg}^{2+}$  and  $\text{K}^+$  (Figure 4) and  $\text{SO}_4^{2-}$   
185 and  $\text{NO}_3^-$  (Figure EA1). Of all these species,  $\text{SO}_4^{2-}$  is the only one that is characterized by a  
186 similar decrease in all the studied spring waters. For cations, the concentration decrease is  
187 relatively weak for  $\text{Mg}^{2+}$  and for  $\text{K}^+$ , but it is much larger for  $\text{Ca}^{2+}$ , and the magnitude of  
188 variation can differ significantly from one spring to another. The decrease in  $\text{Ca}^{2+}$   
189 concentrations is about 20% for CS3, 25% for CS2 and CS4, and it ranges up to 50% for the  
190 CS1 and RH3 springs between 1990 and 2010 (Figure 4). During the same period, pH and  
191 alkalinity have tended to increase in the spring waters. For example, an increase in the mean  
192 annual pH from approximately 5.80 to 6.40 and an increase in the mean alkalinity from 0.017  
193 to 0.030 meq/L were noted for the CS1 spring between 1986 and 2010. The temporal  
194 evolution of  $\text{NO}_3^-$  is different than for the other chemical species.  $\text{NO}_3^-$  concentrations are  
195 similar for all of the springs in 1990 but show different trends after 2004; significant  
196 increases can be seen in some of the CS springs and the RH3 spring (Figure EA1).  $\text{Cl}^-$ ,  $\text{Na}^+$ , and  
197  $\text{H}_4\text{SiO}_4$  are characterized by relatively uniform concentrations within the catchment and by  
198 nearly constant concentrations over the studied period (Figure 4; Figure EA1).

199 The long-term trends observed for the major dissolved species in the spring waters can be  
200 explained by the relative importance of the lithogenic and atmospheric contributions to the  
201 element budgets. The OHGE data indicate that, during the 1986-2010 period, cation and  
202  $\text{H}_4\text{SiO}_4$  concentrations have been relatively stable in the rainwater collected in the  
203 watershed (OHGE data; Figure EA2 and EA3). The  $\text{Mg}^{2+}$  and  $\text{H}_4\text{SiO}_4$  concentrations in the  
204 rainwater are stable and very low ( $<0.01$  mmol/L). The  $\text{Ca}^{2+}$  and  $\text{K}^+$  concentrations are  
205 relatively stable but higher ( $<0.03$  mmol/L), whereas the concentrations of  $\text{Na}^+$  indicate that  
206  $\text{Na}^+$  is the dominant cation in the rainwater ( $<0.04$  mmol/L). In addition, the pH variations in

207 the rainwater show a significant increasing trend (Figure EA4), with a mean annual pH of  
208 4.66 in 1990 and 5.63 in 2010. For the anions, the concentrations of  $\text{Cl}^-$  and  $\text{NO}_3^-$  in the  
209 rainwater are nearly constant, while the  $\text{SO}_4^{2-}$  concentrations tend to decrease over the  
210 same period (Figure EA3).

211 In this context, and given the extremely low Cl content of the granite, the stability and  
212 homogeneity of the concentrations of  $\text{Cl}^-$  in the spring waters is likely to be simply a  
213 consequence of the stable atmospheric deposition. Concerning the decrease in  $\text{SO}_4^{2-}$   
214 concentrations, which is characterized by a comparable magnitude for each spring, the  
215 observation of a simultaneous  $\text{SO}_4^{2-}$  concentration decrease in the rainwater, and with a  
216 similar amplitude, suggests that the variations in the sources are directly induced by the  
217 reduction in atmospheric deposition in the watershed from 1986 to 2010. For  $\text{NO}_3^-$ , the  
218 increase cannot be related to any atmospheric increase in  $\text{NO}_3^-$ , as the  $\text{NO}_3^-$  concentrations  
219 remain stable in the rainwater during the 1986-2010 period (OHGE data, Figure EA3). Rather  
220 than a modification of the atmospheric inputs, the nitrogen cycle could have been affected  
221 by the recent biomass changes related to the forest decline observed in the watershed. The  
222 increase in exported  $\text{NO}_3^-$  may be explained by the tree mortality observed in some parts of  
223 the catchment that was caused by the exceptional drought of 2003 and a recent outbreak of  
224 xylophage insects. Similar increases have also been identified in other forested experimental  
225 catchments after similar perturbations (Knight et al., 1991; Lovett et al., 2002). The role of  
226 vegetation is reinforced by the strong increase in the  $\text{NO}_3^-$  concentrations seen in some of  
227 the soil solution samples collected at the spruce site that cannot be explained by changes in  
228 the concentration of  $\text{NO}_3^-$  in the rainwater, which is stable (OHGE data, Figure EA3). The data  
229 therefore suggest that the temporal evolution of the anion concentrations in the spring  
230 waters are mainly controlled by atmospheric deposition and vegetation cover changes.

231 For the cations and dissolved silica, the budget of these species is controlled by water-rock  
232 interactions within the bedrock and the atmospheric contribution. The importance of the  
233 atmospheric contribution in the Strengbach catchment strongly depends on the species  
234 being considered. It is negligible for  $\text{H}_4\text{SiO}_4$  (<3%), relatively low for  $\text{Mg}^{2+}$  and  $\text{Ca}^{2+}$  (<20%),  
235 and significant for  $\text{Na}^+$  and  $\text{K}^+$  (up to 60%; Viville et al., 2012). The fact that each spring shows  
236 a different decreasing trend for the  $\text{Ca}^{2+}$  concentrations indicates that the evolution of  $\text{Ca}^{2+}$  is  
237 not only related to the variability in atmospheric input, as seen for the  $\text{SO}_4^{2-}$  anion; it also  
238 depends on the reactivity of minerals within the bedrock and the hydrodynamic  
239 characteristics of each spring. At the same time, the constant and uniform concentrations of  
240  $\text{H}_4\text{SiO}_4$  and  $\text{Na}^+$  and the limited variations in  $\text{K}^+$  and  $\text{Mg}^{2+}$  in the spring water point to the  
241 stable functioning of silicate weathering within the bedrock.

#### 242 **4-3-Spatial and temporal variations of the weathering fluxes**

243 Monitoring the geochemical composition and discharge of the Strengbach springs also  
244 allows estimation of the chemical weathering fluxes exported by the different springs during  
245 the 1986-2010 period. This calculation is performed in this study for dissolved silica ( $\text{H}_4\text{SiO}_4$ )  
246 and basic cations ( $\text{K}^+$ ,  $\text{Na}^+$ ,  $\text{Ca}^{2+}$  and  $\text{Mg}^{2+}$ ) using the instantaneous spring water discharges  
247 and the elemental concentrations. The conversion of the net chemical fluxes into specific  
248 weathering fluxes (in  $\text{T}/\text{km}^2/\text{yr}$ ) requires the accurate estimation of the surface areas drained  
249 by the different springs and correct for the atmospheric contributions. This was done by  
250 Viville et al. (2012) for the Strengbach stream at the outlet of the catchment. This is done in  
251 this study for the different springs. The surface areas drained by the Strengbach springs are  
252 assimilated to the small surface areas of the “watersheds” defined by the different springs.  
253 The correction of the atmospheric contribution, including the effect of throughfalls and/or

254 biomass storage on the chemical fluxes carried by the different springs, has been made  
255 following the approach detailed in Viville et al. (2012) for the whole watershed. The  
256 calculated weathering fluxes indicate that from 1986 to 2010, the only chemical fluxes that  
257 vary significantly with time at a decadal scale and from one spring to another are the  $\text{Ca}^{2+}$   
258 fluxes. In accordance to the elemental concentration variations, the  $\text{H}_4\text{SiO}_4$  and  $\text{Na}^+$   
259 weathering fluxes are relatively stables over the studied period. The weathering flux  
260 variations therefore suggest that the recent perturbations recorded in the catchment have  
261 not modified all the primary mineral weathering rates; instead, they may have affected only  
262 Ca-rich minerals, such as apatite, and/or the compositions of the clay minerals. To evaluate  
263 these hypotheses in a quantitative manner, a numerical modeling approach has been  
264 developed to capture the main processes involved in the acquisition and the evolution of the  
265 chemistry of the Strengbach springs. The modeling will focus on the dissolved silica and the  
266 cation concentrations and will be based on the mean annual data from 1990 to 2010.

## 267 **5-Hydrochemical modeling**

### 268 **5-1-KIRMAT model description**

269 The hydrochemical simulations performed in this study employ the 1D thermo-kinetic code  
270 KIRMAT (KInetic Reactions and MAss Transport; Gérard, 1996; Gérard et al., 1998). The  
271 KIRMAT code simultaneously solves equations describing geochemical reactions and  
272 transport mass balances in a saturated porous medium. Mass transport comprises the  
273 effects of convection, diffusion and kinematic dispersion. Chemical reactions include the  
274 dissolution of primary minerals and oxidoreduction reactions, as well as the precipitation of  
275 secondary minerals and clays. Dissolution and precipitation rate calculations are based on

276 the kinetic laws derived from transition state theory (Eyring, 1935; Murphy and Helgeson,  
277 1987). The dissolution rate of a mineral is expressed in KIRMAT as follows (Ngo et al., 2014):

$$278 \quad r_d = k_d * S_m^{eff} * \alpha_{H^+}^n * \left(1 - \left(\frac{Q_m}{K_m}\right)^{n1}\right)^{n2} \quad (1)$$

279 where  $k_d$  is the dissolution rate constant (mol/m<sup>2</sup>/yr),  $S_m^{eff}$  is the reactive surface of the  
280 mineral m (m<sup>2</sup>/kg H<sub>2</sub>O),  $\alpha_{H^+}^n$  is the activity of protons,  $Q_m$  is the ion activity product of the  
281 mineral m,  $K_m$  is the thermodynamic equilibrium constant of the hydrolysis reaction of the  
282 mineral m, and  $n1$  and  $n2$  are exponents that depend on the pH of the solution (Ngo et al.,  
283 2014). To take into account the ionic exchange between water and clays, the clay fraction is  
284 defined in KIRMAT as a solid solution (Tardy and Fritz, 1981). The clay solid solution is  
285 precipitated at thermodynamic equilibrium and is made up of a combination of pure clay  
286 end members. Its composition varies with time, depending on the evolution of the water  
287 chemistry and the bedrock mineralogy during the simulation (Gérard, 1996; Schaffhauser,  
288 2013). The clay solid solution is one of the strengths of the KIRMAT code. It allows the code  
289 to reproduce, at least to first order, the complex coupling between the composition of clays  
290 and the water chemistry through cationic exchanges. This multicomponent solid solution  
291 also aims to reflect the impurity of the precipitating clays during low-temperature water-  
292 rock interactions (Tardy and Fritz, 1981; Fritz, 1985). The algorithm also includes feedback  
293 effects between mineral mass budgets, reactive surfaces, and bedrock porosity evolution  
294 (Ngo et al., 2014). The KIRMAT code has been used in long-term geochemical evolution of  
295 radioactive waste deposits (Marty et al., 2010; Ngo et al., 2014) and the geochemical  
296 modeling of alluvial groundwaters (Lucas et al., 2010) and surface waters (Chabaux et al.,  
297 2017; Lucas et al., 2017).

## 298 **5-2-Modeling strategy**

299 The modeling approach developed in this work has been adapted from previous  
300 hydrochemical studies performed in the Vosges massif and the Rhine graben (Schaffhauser,  
301 2013; Lucas et al., 2010; 2017). Based on the analyses of major elements and Sr-U isotopes,  
302 the recent work undertaken in the Strengbach and in the neighboring Ringelbach  
303 watersheds suggests that, in these granitic catchments, the springs are supplied by waters  
304 with relatively independent water pathways (Schaffhauser et al., 2014; Chabaux et al., 2017).  
305 In this context, the geochemical compositions of the spring waters have been simulated by  
306 considering a simple geometry, i.e., the granitic bedrock has been discretized along the main  
307 slopes with a 1D succession of cells. The chemical and conservative transport equations were  
308 solved simultaneously using these cells. A schematic representation of the modeling strategy  
309 is presented in Figure 5. This modeling approach assumes that there is no influence of  
310 deeper or lateral flow lines, which may induce a mixing with older waters. The length of the  
311 water pathway used to model the water chemistry of each spring has been estimated by  
312 taking the distance between the summit of the appropriate hillside and the emergence point  
313 of each spring. The calculated lengths of the water pathways obtained using this procedure  
314 are likely to be minimum estimates, as the tortuosity of the medium is not accounted for.

315 This modeling scheme also requires us to define the input and the output solutions; the  
316 latter obviously corresponds to the spring waters to be modeled. For the input solutions, and  
317 as the KIRMAT code is not designed to take into account the effect of the vegetation within  
318 the upper soil layers, it is not possible to directly use the rainwater as the input solution. The  
319 alternative approach proposed in this study is to consider the soil solutions collected at the  
320 greatest depths as the input solutions, because these soil solutions integrate the surface

321 processes that occur before the water percolates through the bedrock. Two of the deepest  
322 soil solution locations, HP-70 and VP-60 from the beech and the spruce sites, which are  
323 located on the southern and the northern parts of the watershed, respectively (data from  
324 Prunier et al., 2015), were used in this study as input solutions. The soil solutions measured  
325 at these sites exhibit a significant increase in mean annual pH (from 4.7 to 5.2 and from 4.4  
326 to 4.8 for HP-70 and VP-60) and a strong decrease (by a factor of 10) in the Ca  
327 concentrations between 1990 and 2010 (Figures EA4, EA5, and EA6; Prunier et al., 2015).

328 The hydrochemical modeling of the spring waters also requires estimation of the bedrock  
329 porosity, the thermodynamic and kinetic constants describing mineral dissolution, and the  
330 reactive surfaces of the minerals. Bedrock porosity has been determined by imbibition  
331 experiments and is  $3\pm 0.5$  % for the HPT facies and  $6.8\pm 1.2$  % for the CA facies (El Gh'Mari,  
332 1995). The thermodynamic and kinetic constants for the primary mineral dissolution  
333 reactions and the associated references are given in Electronic Annex in Table EA1 and Table  
334 EA2. A constant temperature of 6°C, which corresponds to the mean annual temperature of  
335 the spring waters (OHGE data), has been used for all the simulations. The thermodynamic  
336 constants at 6°C have been determined by a polynomial interpolation of the existing  
337 constants, and the kinetic constants at 6°C have been recalculated from the activation  
338 energy of the dissolution reactions (Table EA2). The partial pressure of CO<sub>2</sub> is considered to  
339 be higher than the atmospheric partial pressure, as it is commonly measured in the  
340 underground medium, and it is set to a constant and typical value of  $2.5 \times 10^{-3}$  atm (Hinkle,  
341 1994; Bouma et al., 1997). For the estimation of the reactive surfaces, a spherical geometry  
342 is assumed for all the minerals present in the bedrock. The mean sizes of the different  
343 primary minerals are estimated from macroscopic descriptions and observations of thin



344 sections of the bedrock samples. The reactive surface  $S_p$  ( $\text{m}^2 / \text{kg H}_2\text{O}$ ) for a given primary  
345 mineral is thus calculated by:

$$346 \quad S_p = V_p * \frac{S}{V} \quad (2)$$

347 where  $V_p$  is the volume of mineral per kg of  $\text{H}_2\text{O}$  ( $\text{cm}^3 / \text{kg H}_2\text{O}$ ), and  $S$  and  $V$  are the surface  
348 and the volume of the sphere representative of the considered mineral ( $\mu\text{m}^2$  and  $\mu\text{m}^3$ ). The  
349 volume  $V_p$  is obtained by:

$$350 \quad V_p = X * \frac{(1 - w) * \frac{1000}{\rho}}{w} \quad (3)$$

351  
352 where  $w$  is the bedrock porosity,  $\rho$  is the water density ( $\text{g}/\text{cm}^3$ ), and  $X$  is the volumetric  
353 fraction of the considered mineral. The mineral volumetric fractions and the calculated  
354 specific surfaces for the HPT and CA facies are given in Table 1. The mineral apatite is an  
355 exception to this rule. It is characterized by a low abundance and a small grain size. Thus, its  
356 reactive surface cannot be estimated from observations of mineral size, and it has been  
357 adjusted to generate solute  $\text{Ca}^{2+}$  concentrations having the same order of magnitude as the  
358 spring concentrations measured in 1990. For the clay minerals, the choice of the different  
359 clay solid solution end members is based on mineralogical analyses performed in previous  
360 studies using X-ray diffraction, which indicate that illite and montmorillonite/smectite are  
361 the dominant clay minerals in the granite of the Strengbach watershed (Fichter et al., 1998;  
362 Ackerer et al., 2016). The thermodynamic data used for the solid solution end members are  
363 presented in Table EA3. In addition to the clay solid solution, a small amount of illite is  
364 defined as a primary mineral to represent the background clay content acquired during the  
365 hydrothermal alteration of the granite (Table 1).

366 To model the CS springs, which drain the southern and weakly hydrothermally altered part  
367 of the watershed, the HPT facies has been used to describe the bedrock mineralogy (Figure  
368 1, Table 1). The soil solutions from the beech site, which were sampled at a depth of 70 cm  
369 (HP-70), have been used as input solutions for these simulations. For the RH3 spring, which  
370 drains the northern and hydrothermally altered part of the watershed, the CA facies has  
371 been used to describe the bedrock mineralogy (Figure 1, Table 1). The soil solutions from the  
372 spruce site, which were sampled at a depth of 60 cm on the same hill slope (VP-60), have  
373 been used as input solutions. Considering the emerging point of the ARG spring, which is  
374 located downward and in the vicinity of the Strengbach stream, whether the water is coming  
375 from the southern or the northern part of the watershed is not obvious, and these two  
376 hypotheses have been tested in the following.

### 377 **5-3-Modeling of the spatial variability of the spring water chemistry**

378 To assess the factors that control the spatial variability of the spring water chemistry, the  
379 modeling strategy presented in section 5-2 has been applied to simulate the mean chemical  
380 composition of the springs in 1990. To carry out this task, a first set of runs covering 10 years  
381 has been performed that employs the mean chemistry of the soil solutions measured in  
382 1992-1993 as input solutions. The Darcy rate of each spring was adjusted to obtain the best  
383 match between the simulated and the measured pH values and dissolved concentrations.  
384 The adjusted Darcy rates are in accordance with the hydrodynamic parameters obtained  
385 from a 3D hydrogeological model of the Strengbach catchment (Beaulieu et al., 2016).

386 For the four CS springs that drain the weakly hydrothermally altered slopes, the KIRMAT  
387 model is able to capture the cations and the dissolved silica concentrations in 1990 (Figure  
388 6). Moreover, the simulated pH values range from 6.23 to 6.41, and these values are in good

389 agreement with the field measurements, which range from 5.99 to 6.33. The results  
390 therefore indicate that it is possible to account for the slight chemical differences between  
391 the CS springs by only considering the differences in hydrological conditions: the modeling  
392 has been performed with a single bedrock facies (HPT) and the same input soil solution (HP-  
393 70), but the specific length of the water pathway and the water discharge varies among the  
394 springs. In this modeling context, the  $\text{Ca}^{2+}$  in solution is essentially derived from the  
395 dissolution of apatite present in the HPT facies (ranging from  $4.2 \times 10^{-5}$  to  $2 \times 10^{-5}$  mol/yr/kg  
396  $\text{H}_2\text{O}$  and providing 90-95% of the Ca) and secondarily due to the dissolution of anorthite  
397 ( $\approx 1.1 \times 10^{-5}$  mol/yr/kg  $\text{H}_2\text{O}$ , providing about 5-10% of the Ca). The importance of the apatite  
398 dissolution in the Ca budget of the spring waters is in accordance with the results of Sr-Nd  
399 isotopic investigations performed in the Strengbach catchment, which show independently  
400 that most of the Sr and Nd in the spring waters originates from the dissolution of apatite and  
401 lesser amounts of feldspar (see Aubert et al., 2001; Stille et al., 2009). The dissolution of the  
402 albite ( $\approx 1.3 \times 10^{-4}$  mol/yr/kg  $\text{H}_2\text{O}$ , providing 100% of the Na), K-feldspar ( $\approx 1.3 \times 10^{-5}$   
403 mol/yr/kg  $\text{H}_2\text{O}$ , providing 17% of the K) and biotite ( $\approx 5.8 \times 10^{-5}$  mol/yr/kg  $\text{H}_2\text{O}$ , providing  
404 83% of the K and 100% of the Mg) deliver the  $\text{Na}^+$ ,  $\text{K}^+$ , and  $\text{Mg}^{2+}$  cations in solution. The  
405  $\text{H}_4\text{SiO}_4$  is essentially derived from the dissolution of biotite and feldspars (providing 34% and  
406 66% of the Si respectively), as the spring waters are systematically supersaturated with  
407 respect to quartz and muscovite. The results also show that, at the end of the simulations  
408 and for each CS spring, the precipitated clay solid solution is dominated by the Ca-illite, Ca-  
409 montmorillonite and Mg-montmorillonite end members (Figure 7). For each CS spring, both  
410 primary mineral dissolution and clay precipitation rates are higher in the first part than at  
411 the end of the water pathway. Significant differences can be noted in the rates of clay  
412 precipitation and apatite dissolution (up to a factor of 2), and modest differences are noted

413 for the other primary minerals (<5%). The higher variability in the apatite dissolution rates is  
414 due to the fact that it is the only primary mineral out of those used in the simulations that is  
415 affected by changes in pH. Shifts from the acid to the neutral pH-domain occur for the  
416 apatite dissolution along the water pathways (Figure 8a, Table EA2). In the 1990 case, and  
417 for the CS1 spring, approximately the first half of the water pathway belongs to the acid  
418 domain, whereas the second half reflects the neutral pH-domain (Figure 8a). The modeling  
419 results indicate that the apatite dissolution rate can reach  $4.2 \times 10^{-5}$  mol/yr/kg H<sub>2</sub>O under  
420 acidic conditions (pH $\approx$ 4.8), while it does not exceed  $2 \times 10^{-5}$  mol/yr/kg H<sub>2</sub>O under neutral  
421 conditions (pH>5.7). In addition, there is an important evolution of the relative end member  
422 fractions of clay solid solution along the water pathway. Ca-montmorillonite and Mg-  
423 montmorillonite dominate within the first part of the path (80 to 60 % from 0 to about 200  
424 m), and Ca-illite dominates in the second part (30 to 70 % from about 200 to 400 m; Figure  
425 7). The simulations also indicate that the shift from the dominance of Ca-montmorillonite to  
426 the Ca-illite end member coincides approximately with the location of the transition in the  
427 pH domain for apatite dissolution, which suggests a strong coupling between the apatite and  
428 the clay mineral compositions along the water pathways.

429 To model the ARG spring, which is located in the vicinity of the Strengbach stream, the  
430 simulations show that the chemical composition of the ARG spring in 1990 can be easily  
431 reproduced if the water is considered to have come from the southern part of the watershed  
432 (HPT facies, Figure 9); however, the observations cannot be reproduced using the  
433 hydrothermally altered bedrock of the northern slope (CA facies). In addition, and by  
434 considering the HPT facies, the clay solid solution that precipitates during the simulation is  
435 similar to those obtained in the CS spring simulations. This hydrological function is supported  
436 by the similarity between the mean  $^{87}\text{Sr}/^{86}\text{Sr}$  isotope ratio of the ARG spring (0.726680) and

437 those of the CS spring waters, especially the CS1 spring water (0.726677), whereas there are  
438 substantial differences relative to the value of the RH3 spring waters (0.722363; Sr data in  
439 Pierret et al., 2014).

440 For the RH3 spring waters, which drain from the northern part of the watershed (CA facies),  
441 the simulated concentrations of  $\text{Na}^+$ ,  $\text{Mg}^{2+}$  and  $\text{H}_4\text{SiO}_4$  in 1990 are much lower than the  
442 measured concentrations (Figure 9). Furthermore, the  $\text{Ca}^{2+}$  concentration in solution is  
443 clearly overestimated by a factor of two. The hydrothermally altered CA facies, which is used  
444 as the reference bedrock in the modeling of the RH3 spring, is mainly composed of quartz,  
445 muscovite and K-feldspar, but it is lacking in biotite and plagioclase feldspar (Table 1). The  
446 absence of these primary minerals is directly responsible for the lack of  $\text{Na}^+$ ,  $\text{Mg}^{2+}$  and  $\text{H}_4\text{SiO}_4$   
447 in solution. The overestimation of  $\text{Ca}^{2+}$  is driven by the lower clay precipitation rate in this  
448 configuration. This reduced rate results from the lower rate of silica release from the  
449 dissolution of primary minerals. In this case, the divergence between the simulated and  
450 measured parameters indicates that the hydrothermally altered CA facies is not effective in  
451 reproducing the chemistry of the RH3 spring. One of the reasons that could be proposed to  
452 explain this discrepancy is that the CA facies may not be representative of the bedrock of the  
453 whole hillslope drained by the RH3 spring. In fact, total disappearance of biotite and  
454 plagioclase feldspar corresponds to the highest degree of hydrothermal alteration, which is  
455 probably only locally achieved within the northern part of the watershed. By moderating the  
456 degree of hydrothermal alteration of the CA facies and testing the possibility that small  
457 amounts of plagioclase feldspar (7%) and biotite (2%) are still present in the bedrock (the  
458 modified facies is indicated as CA\* in Table 1), the simulated chemical properties are more  
459 consistent with the field data (Figure 9). This test likely indicates that less hydrothermally  
460 altered regions of the bedrock and/or some uncharacterized hydrothermal minerals might

461 play an important role in the acquisition of the RH3 spring chemistry. Further modeling of  
462 the spring waters draining the northern part of the watershed likely requires a better  
463 mineralogical description of the bedrock of the northern slope to correctly model the  
464 geochemical composition of the RH3 spring waters.

#### 465 **5-4-Response of the CS and ARG springs to modification of the soil solution chemistry**

466 Given the results of the modeling of the spatial variability, the modeling of the temporal  
467 evolution has focused on the CS and the ARG springs, which are located within the southern  
468 part of the watershed, where the chemical composition of the spring water in 1990 has been  
469 correctly modeled. To simulate the response induced by a modification of the soil solution  
470 composition on the spring water chemistry, a second set of simulations has been performed  
471 with the soil solution measured in 2010 as the input solution to the system obtained from  
472 the previous simulations for 1990. The bedrock mineralogical properties at the end of the  
473 simulations in 1990, including the precipitated clay fractions, have been used to define the  
474 initial state for these new simulations. The hydrological parameters, such as the rates of  
475 water flow and the lengths of the flow paths, were assumed to remain unchanged between  
476 1990 and 2010. This assumption is supported by the absence of significant trends in the  
477 mean annual water discharges of the different springs during this period (OHGE data, Viville  
478 et al., 2012). The simulations performed with this approach, which implies an abrupt change  
479 in the soil solution chemistry, is more schematic than the reality, as the soil solutions have  
480 also varied within the studied period. However, the geochemical variations in the soil  
481 solution compositions are not monotonic from 1990 to 2010. For instance, the time  
482 evolution of the chemical compositions of the soil solution HP-70 within the beech plot is  
483 rather smooth from 1993 and 1998 and much larger after 2003, especially in terms of pH

484 and the  $\text{Ca}^{2+}$ ,  $\text{K}^+$  and  $\text{Mg}^{2+}$  concentrations (Prunier et al., 2015; Figure EA4, EA5, EA6). Thus,  
485 even if the simulations cannot precisely reproduce the temporal evolution of the spring  
486 chemistry between 1990 and 2010, they should give a relatively realistic indication of the  
487 mechanisms involved in the response of the spring water chemistry to a modification of the  
488 incoming soil solution compositions, as well as the time required for the system to reach a  
489 new equilibrium state.

490 A first important result of the above modeling approach is to show that a new equilibrium  
491 state is reached relatively quickly, i.e., in less than 5 years after the modification of the soil  
492 solution chemistry. The simulations also indicate that the dissolution rates of biotite and  
493 feldspar decrease only slightly between the two periods, explaining relative stability of the  
494  $\text{K}^+$ ,  $\text{Mg}^{2+}$ ,  $\text{Na}^+$  and  $\text{H}_4\text{SiO}_4$  concentrations during the studied period. On the other hand, the  
495 modifications induced by the pH increase and the  $\text{Ca}^{2+}$  concentration decrease in the soil  
496 solutions significantly affect the behaviors of apatite and the clay minerals. As the pH of the  
497 soil solutions increase significantly between 1990 and 2010 (from about 4.7 to 5.2 for HP-  
498 70), the lengths of the water pathways characterized by rapid dissolution of apatite are  
499 shorter in 2010, while the neutral domains of apatite dissolution are longer (Figure 8b). As a  
500 result, for the CS1 spring, the average apatite dissolution rate along the water pathways  
501 decreases by approximately 20% between 1990 and 2010. For the clay minerals, it is not the  
502 precipitation rate of the clay solid solution which is modified; instead, the composition of the  
503 precipitated clay solid solution changes significantly from 1990 to 2010 (Figure 7). Based on  
504 the simulation results, the increase in pH and the decrease in  $\text{Ca}^{2+}$  concentrations in the soil  
505 solutions produce lower proportions of Ca-montmorillonite and Mg-montmorillonite in the  
506 first part of the water path (30 % from 0 to 80 m) and a larger amount of Ca-illite in the  
507 second part (30 to 80 % from 80 to 400 m; Figure 7). As in the 1990 case, the shift between

508 the dominance of the Ca-montmorillonite end member to that of the Ca-illite end member  
509 corresponds approximately to the shift in the pH-domain related to apatite dissolution. Such  
510 an evolution of the composition of the clay solid solution implies that the Ca content of the  
511 clay minerals increases by 10% for the CS1 spring between 1990 and 2010. The modeling  
512 results thus indicate that modifications to the soil solution chemistry impact both the apatite  
513 dissolution rates and the incorporation of Ca in the clay mineral structures, which  
514 progressively modifies the chemical composition of the water along its path within the  
515 bedrock.

516 When comparing the chemical trends along a water pathway after a perturbation with an  
517 unperturbed system, it is interesting to note that both cases will lead to the same final  
518 steady state concentration. For the Strengbach case, such a steady state is achieved after the  
519 water has traversed a relatively long pathway within the bedrock, much longer than the  
520 lengths of the water pathways assumed for the simulations of the different springs. This is  
521 why the variations in the incoming soil solutions have a substantial impact on the emerging  
522 spring waters. However, the water/rock interactions highlighted in the previous simulations  
523 progressively dampen the perturbations induced by the soil solution changes. Because the  
524 chemical compositions of the CS and the ARG springs have been modeled with the same  
525 bedrock facies, the attenuation of the perturbation is a function only of the mean water  
526 residence time, which is controlled by the length of flow path and the discharge of the  
527 springs. For the CS1 spring, which is characterized by a shorter water residence time, the soil  
528 solution changes have an important impact on both the apatite dissolution and the  
529 composition of the clays, leading to a strong decrease in the simulated  $\text{Ca}^{2+}$  concentrations  
530 between 1990 and 2010. For the other CS springs and the ARG spring, the same mechanisms  
531 are involved in the decrease in the  $\text{Ca}^{2+}$  concentrations, but the magnitude of the decrease is



532 shaped by the different hydrological conditions and water pathways (Figure 10). For  
533 example, the CS2, CS4 and ARG springs, which emerge at a lower altitude than the CS1  
534 spring, exhibit a smaller decrease in the  $\text{Ca}^{2+}$  concentrations, as the longer water pathways of  
535 these springs moderate the impact of the soil solution changes. For the CS3 spring, it is the  
536 lower water flow rate of this spring which dampens the variations in the soil solutions by  
537 increasing the water/rock interaction time.

538 In this context, the simulated concentrations show that the KIRMAT code captures the  
539 particular chemical evolution of the CS springs from 1990 to 2010, i.e., the significant  
540 decrease in  $\text{Ca}^{2+}$  and the relative stability or the slight decrease in dissolved silica and the  
541 other cations (Figure 11). A test simulation has been performed in which the precipitation of  
542 clay minerals in the granitic bedrock has been prevented. Without any clay precipitation, the  
543 test simulation indicates that the pH of the spring water stabilizes rapidly along the water  
544 pathways and above the pH of the apatite neutral domain ( $\text{pH}>6$ ). In this extreme case, the  
545 apatite dissolution rate varies less over the studied period, and the model is not able to  
546 reproduce the decrease in  $\text{Ca}^{2+}$  between 1990 and 2010. Together, these modeling results  
547 show (1) that the decrease in  $\text{Ca}^{2+}$  in the spring water is explained by the evolution of the soil  
548 solution chemistry and the interactions between the apatite and the clay minerals, and (2)  
549 the relative stability of the other cations and the dissolved silica is due to the weak variations  
550 in the dissolution rates of other primary minerals and the stability of the bulk precipitation  
551 rates of the clay minerals.

552 The modeling results obtained in this study therefore support the views that clay minerals  
553 should not be considered as inert products of weathering processes and that the  
554 precipitation of clays, which impact spring water chemistry, is also a factor that controls the

555 dissolution rates of primary minerals. Such interactions between the primary and the  
556 secondary minerals are in accordance with the results from previous studies that involve  
557 numerical modeling of soil profile development (Maher et al., 2009) or the chemistry of soil  
558 solutions in the Strengbach catchment (Goddéris et al., 2006). At the same time, the results  
559 obtained in this study show that the temporal evolution of the spring chemistry cannot be  
560 explained solely by variations in clay mineral compositions, i.e., simple modifications of the  
561 chemical composition of the precipitated clays or the ionic exchange capacity of the clay  
562 minerals. Instead, the interrelations between the changes in the apatite dissolution rate and  
563 the clay mineral compositions are definitely involved.

## 564 **6-Discussion and geochemical implications**

### 565 **6-1-Spatial and temporal uniformity of the weathering fluxes**

566 In addition to the modeling of the water-rock interactions along the flow path in the aquifer,  
567 monitoring the geochemical composition and discharge of the Strengbach springs allows to  
568 discuss the variability of the chemical fluxes exported by the different springs during the  
569 1986-2010 period. The results show an almost perfect correlation between the calculated  
570 chemical fluxes and the water discharges for all the Strengbach springs (Figure 12). The data  
571 also highlight that even if the substratum includes slight lithological variations, the chemical  
572 fluxes exported for a given water discharge are highly comparable from one spring to  
573 another (Figure 12). This observation likely means that the nature of the primary minerals  
574 and the weathering phases involved in the water-rock interactions controlling the chemical  
575 fluxes exported by the different springs must be relatively similar within the Strengbach  
576 catchment. This interpretation can certainly be extended to the other catchments exhibiting  
577 weak lithological variations and relatively stable chemical compositions for several spring or

578 stream waters. This conclusion is also consistent with modeling results, which show that the  
579 chemical compositions of the CS and ARG springs can be correctly described using the same  
580 mineralogical assemblages. For the RH3 spring, which is located within the northern part of  
581 the catchment, the inability of the model to precisely capture the chemical composition of  
582 this spring complicates the explanation of the comparable exported fluxes. At this stage, and  
583 based on the similarity of the exported fluxes from the springs between the two parts of the  
584 watershed, it might be proposed that the lithological variations within the catchment have a  
585 relatively limited impact on the nature of the weathering reactions controlling the solute  
586 concentrations of  $\text{H}_4\text{SiO}_4$  and  $\text{Na}^+$ , which are the two dominant chemical species of the  
587 dissolved loads carried by the Strengbach springs. As it is also apparent from the chemical  
588 evolution of the spring waters, the only chemical fluxes that vary significantly with time and  
589 from one spring to another are the  $\text{Ca}^{2+}$  fluxes. However, because the contribution of  $\text{Ca}^{2+}$  to  
590 the total weathering fluxes is modest (<10%), and due to the relative stability of the  
591 concentrations of dissolved silica and other cations, the global weathering fluxes exported  
592 by the springs remain relatively stable over the studied period. Thus, even if the watershed  
593 has been affected by recent perturbations that are reflected in the chemistry of the soil  
594 solutions (Prunier et al., 2015), and that have affected the  $\text{Ca}^{2+}$  concentrations and fluxes of  
595 the spring waters (this study), the total chemical fluxes carried by the springs have only  
596 varied slightly from 1990 to 2010. The absence of extensive anthropization, pesticide, and  
597 agricultural spreading within the Strengbach watershed may also explain this stability.

## 598 **6-2 Chemostatic behavior of the Strengbach springs**

599 The relative stability of the chemical concentrations over a wide range of water discharge is  
600 not unique to the Strengbach catchment. This “near-chemostatic” behavior has been

601 described in other experimental catchments where the exported fluxes are nearly  
602 proportional to the water discharges (Godsey et al., 2009; Clow and Mast, 2010; Thompson  
603 et al., 2011). Different mechanisms have been hypothesized to explain the stability of the  
604 solute concentrations in natural waters. For instance, based on the observation that mineral  
605 weathering rates are directly dependent on reactive mineral surfaces (Lasaga et al., 1994), it  
606 has been proposed that the relationship between concentrations and discharges may result  
607 from a change in the reactive mineral surface area in response to changing hydrologic  
608 conditions (Godsey et al., 2009; Clow and Mast, 2010). Among different scenarios, vertical  
609 expansion of the saturated zone and hence an increase in the reactive mineral surface areas  
610 in contact with groundwater might be envisaged during snowmelt or rainfall events. On the  
611 other hand, during drought events associated with low discharge periods, the reactive  
612 mineral surface area would decrease (Clow and Mast, 2010). Alternatively, the chemostatic  
613 behavior of small catchments has been interpreted by considering that the fluid residence  
614 time in the watersheds is long enough for the stream to reach an equilibrium concentration,  
615 which means, that the length scale of the water pathway in the catchments is longer than  
616 the distance required for the fluid to reach a chemical equilibrium between dissolution of  
617 primary minerals and precipitation of secondary minerals (Maher, 2010; 2011).

618 The numerical approach developed in this work allows characterization of the evolution of  
619 the water chemical composition along the flow paths. Therefore, the relevance of the above  
620 scenarios in explaining the chemostatic behavior of the Strengbach springs can be discussed.  
621 The simulation results show unambiguously that the pathway length needed to reach an  
622 equilibrium concentration is much longer than those estimated within the catchment for the  
623 different springs. As an illustration, based on the simulations of the CS1 spring waters, a  
624 distance as long as 15-20 km is required for the water to reach an equilibrium concentration

625 of approximately  $1.7 \times 10^{-3}$  mol/L for  $\text{Ca}^{2+}$  (Figure 10), and of about  $1.9 \times 10^{-3}$  mol/L for  
626  $\text{H}_4\text{SiO}_4$  (not shown). Taken as such, these results imply that the chemostatic behavior of the  
627 Strengbach springs cannot be explained by the mobilization of waters close to a chemical  
628 equilibrium state. Other scenarios must be invoked, such as an hydrological control implying  
629 a relative similarity of the water residence times feeding individual springs, regardless of  
630 discharge. Large water storage within the substratum, which can be envisaged for the  
631 Strengbach catchment (Viville et al., 2006), associated with rapid hydrological response of  
632 the aquifer to rainwater inputs may account for such a behavior. The hydrological  
633 interpretation for the Strengbach chemostatic behavior is reinforced by the consistency  
634 between some modeling results and field data. Firstly, the amount of precipitated clay is  
635 realistic compared to field observations. A test simulation performed over approximately 20  
636 kyr produced a mass fraction of clay minerals of 2-3% in the first part of the water pathway  
637 of the CS1 spring. The duration of 20 kyr corresponds approximately to the recent  
638 weathering stage of the granitic bedrock since the last glacial maximum (Ackerer et al.,  
639 2016). This is consistent with the fraction of  $\approx 2\%$  of clay minerals determined by X-ray  
640 diffraction analysis in the granitic basement of the weathering profiles located within the  
641 southern part of the Strengbach catchment (Fichter et al., 1998; Ackerer et al., 2016).  
642 Secondly, in our modeling work, the end members of the clay solid solution are relevant and  
643 have been selected on the basis of X-ray diffraction analyses of bedrock samples collected in  
644 the field (Fichter et al., 1998; Ackerer et al., 2016). A different choice of the precipitating clay  
645 minerals would modify both the chemical compositions and the chemical equilibrium lengths  
646 of the spring waters. For example, a test simulation that only considers that small amount of  
647 kaolinite is precipitating, as in Maher (2009, 2010), shows that an equilibrium concentration  
648 for  $\text{H}_4\text{SiO}_4$  is achieved within only about 300 m along the water pathways (not shown). In the

649 extreme case, in which clay precipitation is totally prevented, the equilibrium concentration  
650 would be achieved in less than 200 m along the water pathways. Nevertheless, these two  
651 theoretical cases are not able to capture the chemical evolution of the springs between 1990  
652 and 2010, in contrast to the simulations made with the secondary clay mineral assemblages  
653 retained in our study. Thus, at this stage, the only parameters that may impact our  
654 interpretation for the chemostatic behavior of the Strengbach springs are the values  
655 employed for the kinetic constants of the primary mineral dissolution reactions. For all of the  
656 simulations, the kinetic constants of the primary mineral dissolution reactions are those  
657 determined through laboratory experiments (Table EA2), following procedures used in other  
658 modeling studies (e.g., Godd ris et al., 2006). Such experimental values may overestimate  
659 field values (White and Brantley, 2003). Different possibilities have been proposed to explain  
660 the apparent discrepancy between experimental and field data, such as, for instance, a  
661 physical occlusion of the primary minerals by secondary phases (White and Brantley, 2003)  
662 or the development of amorphous silica-rich layers on the mineral surfaces (Daval et al.,  
663 2011; Wild et al., 2016). Accordingly, some modeling studies have adjusted and decreased  
664 the kinetic constants of the primary mineral dissolution reactions (e.g., Maher, 2009; 2010;  
665 Lucas et al., 2017). Adjusting kinetic constants will result in different dissolution rates of the  
666 primary minerals, and thus in different chemical equilibrium lengths of the spring waters.  
667 However, in the Strengbach case, the ability of the simulations to capture the spatial  
668 variability and the time evolution of the spring water chemistry do not encourages us to  
669 modify the kinetic constants used for the simulations. Hence, our results suggest that the  
670 chemostatic behavior of the Strengbach springs is explained by an hydrological control of the  
671 water residence times feeding individual springs, rather than a scenario assuming chemical  
672 equilibrium state. We are nevertheless fully aware that the definitive choice between these

673 different schemes, whatever the considered catchments, will be based on our future ability  
674 to correctly estimate the kinetic constants of dissolution of primary minerals and  
675 precipitation of secondary minerals in the natural environment.

### 676 **6-3-Comparison of current and long-term weathering rates**

677 The calculation of the weathering fluxes exported by the springs enables comparison of the  
678 current weathering rates with the long-term ones determined along a regolith profile  
679 located on the summit of the southern part of the catchment (Ackerer et al., 2016). This  
680 profile is located on the same slope as the CS springs and integrates the chemical losses  
681 associated with regolith formation over the last 20 kyr (Ackerer et al., 2016). The calculated  
682 current and long-term weathering rates are given in the Table 2. The results indicate that,  
683 whatever parameter values are used for the atmospheric correction, there is a good  
684 consistency between the current  $\text{H}_4\text{SiO}_4$  weathering fluxes estimated for the four CS springs  
685 and the long-term ones (approximately 2-3 T/km<sup>2</sup>/yr). These estimates are also quite  
686 consistent with the current fluxes of 2.89 T/km<sup>2</sup>/yr for  $\text{H}_4\text{SiO}_4$  determined at the watershed  
687 scale in the Strengbach stream (Viville et al., 2012). Given the uncertainty and the  
688 assumptions made in performing the atmospheric contribution corrections, the data also  
689 suggest a good agreement between the current and the long-term weathering fluxes of  $\text{Na}^+$ .  
690 On the other hand, for  $\text{Mg}^{2+}$ ,  $\text{Ca}^{2+}$  and  $\text{K}^+$ , the current weathering fluxes determined for the  
691 springs and the stream waters are different from the long-term estimates. Substantially  
692 higher current rates are obtained for  $\text{Ca}^{2+}$ , slightly higher ones are obtained for  $\text{Mg}^{2+}$  and  
693 lower ones are obtained for  $\text{K}^+$  (Table 2). For  $\text{Ca}^{2+}$ , the difference between the long-term and  
694 the current estimates ranges from a factor of 4 to 18, as both the long-term estimates and  
695 the current atmospheric corrections contain substantial uncertainties.

696 The modeling approach presented in this work can be used to discuss the origins of such  
697 differences. By only considering a modification of the two main parameters that are involved  
698 in explaining the 20-year variations, namely the modification of the pH and the  
699 concentrations of  $\text{Ca}^{2+}$  in the soil solutions, the modeling results demonstrate that it is not  
700 possible to explain the observed decreases in the fluxes of  $\text{Ca}^{2+}$  exported by the different  
701 springs. A 4 to 18-fold difference between the long-term and the current weathering fluxes  
702 for  $\text{Ca}^{2+}$  thus requires a modification of the other bio-climatic parameters of the weathering  
703 system, especially the water temperature, the partial pressure of  $\text{CO}_2$  ( $p\text{CO}_2$ ) and the water  
704 flows. To reproduce in a schematic manner the climatic conditions that are thought to have  
705 prevailed in the watershed before the warming associated with the onset of the Holocene, a  
706 simulation has been performed in which a cooling from  $6^\circ\text{C}$  to  $1^\circ\text{C}$  for the spring water  
707 temperatures, a higher pH of 5.7 for the soil solutions, and a lower partial pressure of  $\text{CO}_2$   
708 that corresponds to a pre-anthropogenic atmospheric level (200 ppmv) are considered. Such  
709 pH and  $p\text{CO}_2$  values for the deeper soil solutions and the percolating bedrock waters are  
710 those expected for a system without any biological activity in the soil, which is clearly an  
711 extreme situation. Under such conditions, the apatite weathering rate decreases in response  
712 to the lower temperature and  $p\text{CO}_2$  values, and the simulated  $\text{Ca}^{2+}$  concentrations are  
713 approximately divided by a factor of 4 in the spring waters with respect to 1990 (Figure 13).  
714 Because drier conditions prevailed during the last glacial maximum in central Europe  
715 (Sirocko et al., 2016), lower water flows likely prevailed in the Strengbach watershed in the  
716 past, which would decrease the exported fluxes of  $\text{Ca}^{2+}$  even further and explain the 4 to 18-  
717 fold differences. Interestingly, the simulated  $\text{H}_4\text{SiO}_4$  and  $\text{Na}^+$  concentrations are less sensitive  
718 to the temperature and the  $p\text{CO}_2$  changes than the  $\text{Ca}^{2+}$  concentrations, and they only vary  
719 by 20% between the simulations representing past and current conditions. These findings



720 are also in accordance with the geochemical dataset and the 1990-2010 modeling results,  
721 which show that the  $\text{Ca}^{2+}$  concentrations in the Strengbach spring waters are much more  
722 strongly affected by the recent superficial perturbations than the  $\text{H}_4\text{SiO}_4$  and the  $\text{Na}^+$   
723 concentrations over decadal timescales. Taken together, these different results suggest that,  
724 in a granitic catchment such as the Strengbach watershed, the silicate weathering processes  
725 are little affected by environmental changes, both at the millennial time scale of Quaternary  
726 climatic changes and at the multi-annual scale of recent environmental changes. Only  
727 chemical elements such as  $\text{Ca}^{2+}$ , for which the budget in the spring waters is controlled by  
728 the behavior of the clays and of minor minerals such as apatite, and elements such as  $\text{K}^+$ ,  
729 which are strongly affected by the dynamics of the biological processes, are significantly  
730 impacted by the environmental changes.

### 731 **Conclusion**

732 This study highlights the potential of combining monitoring data and the hydrochemical  
733 modeling of surface waters to investigate the variability of the weathering processes within  
734 a small watershed. The KIRMAT simulations demonstrate that the significant decrease in the  
735  $\text{Ca}^{2+}$  concentrations in the spring waters is a reflection of both the dissolution rate variability  
736 of the apatite mineral and the changes in clay composition in response to the evolution of  
737 the input soil solution. The results also indicate that the magnitude of the changes in  $\text{Ca}^{2+}$   
738 concentrations is shaped by the different hydrological conditions and the specific water  
739 residence time of each spring. Apart from the important pH and  $\text{Ca}^{2+}$  concentration changes,  
740 the simulations also account for the weak variability in the  $\text{Na}^+$  and the  $\text{H}_4\text{SiO}_4$  concentrations  
741 and explain the relative stability of the global weathering fluxes exported by the springs  
742 during the studied period. Our results furthermore suggest that the chemostatic behavior of

743 the Strengbach springs is explained by an hydrological control of the water residence times  
744 feeding individual springs, rather than a scenario assuming chemical equilibrium state. This  
745 conclusion for the Strengbach site, but also for any other hydrological contexts, depends on  
746 our ability to correctly estimate the kinetic constants of both the primary mineral dissolution  
747 and the clay mineral precipitation. Finally, the comparison between the current and the  
748 long-term weathering rates determined from the spring water monitoring and along a  
749 regolith profile shows that the modern chemical fluxes of  $\text{Ca}^{2+}$  are higher than the long-term  
750 ones, while the relative stability of the silicate weathering processes is probably true over a  
751 long time scale. These different results indicate that silicate weathering processes are  
752 characterized by a weak spatial and temporal variability, whereas chemical species such as  
753  $\text{Ca}^{2+}$ , for which the budget in the spring waters is controlled by the behavior of the clays and  
754 of minor minerals such as apatite, are significantly impacted by the current environmental  
755 changes, as well as Quaternary climatic changes.

756 **Acknowledgements:** This work was supported by a Ph. D. scholarship awarded to J. Ackerer  
757 by the Region Alsace, France and the BRGM, Orléans, France. It was financially supported by  
758 funding from the CPER-Alsace REALISE program, and by the French ANR Program under  
759 grant agreement ANR-15-CE06-0014 (Projet CANTARE- Alsace) and grant agreement ANR-15-  
760 CExx. Yves Godderis is warmly thanked for very constructive and positive comments on a  
761 preliminary version of this work, which also benefited from fruitful discussions with P. Stille  
762 and J. van der Woerd. This is a LHyGeS-EOST contribution.

763 **Figure captions**

764 Figure 1: sampling locations within the Strengbach catchment. Stars, circles, diamonds and triangles  
765 represent the springs, the soil solutions, the bedrock facies and the weathering profiles respectively.

766 Figure 2: (a) spatial variability of the  $\text{Ca}^{2+}$  and  $\text{Mg}^{2+}$  concentrations for the different springs emerging  
767 in the Strengbach catchment (b) seasonal variability and decadal evolution of the  $\text{Ca}^{2+}$  and the  $\text{H}_4\text{SiO}_4$   
768 concentrations for spring CS1 between 1990 and 2012.

769 Figure 3: temporal evolution of the concentrations of cations ( $\text{Na}^+$ ,  $\text{K}^+$ ,  $\text{Ca}^{2+}$ ,  $\text{Mg}^{2+}$ ), anions ( $\text{SO}_4^{2-}$ ,  $\text{NO}_3^-$ ,  
770  $\text{Cl}^-$ ) and dissolved silica ( $\text{H}_4\text{SiO}_4$ ) measured at the CR spring collector from 1990 to 2010.

771 Figure 4: temporal evolution of the concentrations of cations ( $\text{Na}^+$ ,  $\text{K}^+$ ,  $\text{Ca}^{2+}$ ,  $\text{Mg}^{2+}$ ) and dissolved silica  
772 ( $\text{H}_4\text{SiO}_4$ ) for the different CS, ARG and RH3 springs from 1990 to 2010.

773 Figure 5: conceptual scheme used in the modeling. The granitic bedrock is discretized into a 1D  
774 succession of cells along the water path, and soil solutions are used as input solutions. For a given  
775 cell M, the concentration variation  $\Delta C_e$  for an element e is calculated from geochemical and  
776 transport fluxes. The output solutions produced by the system are considered to represent the spring  
777 waters that are to be modeled.

778 Figure 6: simulation of the CS springs in 1990 with the HPT facies. Blue and red bars represent the  
779 modeled and the measured elemental concentrations of the CS springs. Gray bars represent the  
780 measured concentrations of the soil solution HP-70 in 1992.

781 Figure 7: relative fractions of the different end members of the clay solid solution along the water  
782 pathway. The results are presented for the CS1 spring in 1990 (a) and in 2010 (b).

783 Figure 8: evolution of the simulated pH along the water pathway for the CS1 spring in 1990 and 2010.  
784 The modeling results allow identification of two distinct zones: (1) a zone with  $\text{pH} < 6$  that is  
785 characterized by rapid apatite dissolution and the dominance of Ca-montmorillonite and (2) a zone  
786 with  $\text{pH} > 6$  that is characterized by slower apatite dissolution and the dominance of Ca-illite.

787 Figure 9: simulation of the ARG spring in 1994 and 2008 with the HPT facies and the RH3 spring in  
788 1990 with the CA and the CA\* facies. Blue and red bars represent the modeled and the measured  
789 elemental concentrations of the spring waters. Gray bars represent the measured concentrations of  
790 the soil solution HP-70 for the simulation of ARG and the measured concentrations of the soil  
791 solution VP-60 for the simulation of RH3.

792 Figure 10: evolution of the simulated  $\text{Ca}^{2+}$  concentrations along the water pathways for the CS1 and  
793 CS2 springs in 1990 and 2010. The different water residence times imply different responses of the  
794  $\text{Ca}^{2+}$  concentrations to changes in the soil solution. The CS3 and CS4 springs are not represented in  
795 this figure for reasons of clarity, but the same mechanisms are involved. The results are also shown  
796 for the CS1 spring in 1990 and 2010 along a theoretical water pathway of 20 km.

797 Figure 11: simulation of the CS springs in 2010 with the HPT facies. Blue and red bars represent the  
798 modeled and the measured elemental concentrations of the CS springs. Gray bars represent the  
799 measured concentrations of the soil solution HP-70 in 2010.

800 Figure 12: chemical weathering fluxes of cations ( $\text{Na}^+$ ,  $\text{K}^+$ ,  $\text{Ca}^{2+}$ ,  $\text{Mg}^{2+}$ ) and dissolved silica for the  
801 different springs from 1990 to 2010.

802 Figure 13: evolution of the simulated  $\text{Ca}^{2+}$  concentrations along the water pathways for the CS1  
803 spring in the recent periods and in the 20 000 years before the present day. The domain of the  
804 concentrations corresponding to the long-term estimates is represented by the black rectangle.

#### 805 **Table captions**

806 Table 1: mineralogical compositions and reactive surfaces for the different bedrock facies used in this  
807 study (i.e., the HPT, CA and CA\* facies).

808 Table 2: Estimated chemical fluxes for the different CS springs (1990-2010) and for the studied  
809 regolith profile. (F) uncorrected. (A) corrected for atmospheric deposition. (B) corrected for  
810 atmospheric deposition and tree harvesting. (C) corrected for atmospheric deposition and tree

811 growth. The corrections were calculated using the method presented in Viville et al., 2012. The  
812 chemical species are not impacted in the same way by the different possible corrections because the  
813 atmospheric contribution depends on how the elements are concentrated in the rainwater and is  
814 affected by biomass cycling. As an example, these factors are much more important for  $K^+$  than for  
815 the dissolved silica ( $H_4SiO_4$ ).

## 816 **References**

- 817 Ackerer, J., Chabaux, F., Van der Woerd, J., Viville, D., Pelt, E., Kali, E., ... & Négrel, P. (2016).  
818 Regolith evolution on the millennial timescale from combined U–Th–Ra isotopes and  
819 in situ cosmogenic  $^{10}Be$  analysis in a weathering profile (Strengbach catchment,  
820 France). *Earth and Planetary Science Letters*, 453, 33-43.
- 821 Aubert, D., Stille, P., & Probst, A. (2001). REE fractionation during granite weathering and  
822 removal by waters and suspended loads: Sr and Nd isotopic evidence. *Geochimica et*  
823 *Cosmochimica Acta*, 65(3), 387-406.
- 824 Beaulieu, E., Goddérís, Y., Labat, D., Roelandt, C., Oliva, P., & Guerrero, B. (2010). Impact of  
825 atmospheric  $CO_2$  levels on continental silicate weathering. *Geochemistry,*  
826 *Geophysics, Geosystems*, 11(7).
- 827 Beaulieu, E., Goddérís, Y., Donnadieu, Y., Labat, D., & Roelandt, C. (2012). High sensitivity of  
828 the continental-weathering carbon dioxide sink to future climate change. *Nature*  
829 *Climate Change*, 2(5), 346-349.
- 830 Beaulieu, E., Lucas, Y., Viville, D., Chabaux, F., Ackerer, P., Goddérís, Y., & Pierret, M. C.  
831 (2016). Hydrological and vegetation response to climate change in a forested  
832 mountainous catchment. *Modeling Earth Systems and Environment*, 2(4), 191.

833 Bouma, T. J., Nielsen, K. L., Eissenstat, D. M., & Lynch, J. P. (1997). Soil CO<sub>2</sub> concentration  
834 does not affect growth or root respiration in bean or citrus. *Plant, Cell &*  
835 *Environment*, 20(12), 1495-1505.

836 Chabaux, F., Viville, D., Lucas, Y., Ackerer, J., Ranchoux, C., Bosia, C., ... & Lerouge, C. (2017).  
837 Geochemical tracing and modeling of surface and deep water–rock interactions in  
838 elementary granitic watersheds (Strengbach and Ringelbach CZOs, France). *Acta*  
839 *Geochimica*, 36, 363–366.

840 Clow, D. W., & Mast, M. A. (2010). Mechanisms for chemostatic behavior in catchments:  
841 implications for CO<sub>2</sub> consumption by mineral weathering. *Chemical Geology*, 269(1),  
842 40-51.

843 Dambrine, E., Pollier, B., Poszwa, A., Ranger, J., Probst, A., Viville, D., ... & Granier, A. (1998).  
844 Evidence of current soil acidification in spruce stands in the Vosges Mountains, north-  
845 eastern France. *Water, Air, and Soil Pollution*, 105(1-2), 43-52.

846 Daval, D., Sissmann, O., Menguy, N., Saldi, G. D., Guyot, F., Martinez, I., ... & Hellmann, R.  
847 (2011). Influence of amorphous silica layer formation on the dissolution rate of  
848 olivine at 90 C and elevated pCO<sub>2</sub>. *Chemical Geology*, 284(1), 193-209.

849 Donnini, M., Frondini, F., Probst, J. L., Probst, A., Cardellini, C., Marchesini, I., & Guzzetti, F.  
850 (2016). Chemical weathering and consumption of atmospheric carbon dioxide in the  
851 Alpine region. *Global and Planetary Change*, 136, 65-81.

852 Egli, M., Mirabella, A., & Sartori, G. (2008). The role of climate and vegetation in weathering  
853 and clay mineral formation in late Quaternary soils of the Swiss and Italian Alps.  
854 *Geomorphology*, 102(3), 307-324.

855 El Gh'Mari, A. (1995). Étude pétrographique, minéralogique et géochimique de la dynamique  
856 d'altération d'un granité soumis aux dépôts atmosphériques acides (bassin versant du

857 Strengbach, Vosges, France): mécanisme, bilan et modélisation, en dépôt à la Soc.  
858 géol. France Thèse Université Louis-Pasteur, 200.

859 Eyring, H. (1935). The activated complex in chemical reactions. *The Journal of Chemical*  
860 *Physics*, 3(2), 107-115.

861 Fichter, J., Turpault, M. P., Dambrine, E., & Ranger, J. (1998). Mineral evolution of acid forest  
862 soils in the Strengbach catchment (Vosges Mountains, NE France). *Geoderma*, 82(4),  
863 315-340.

864 Fritz, B. (1985). Multicomponent solid solutions for clay minerals and computer modeling of  
865 weathering processes. In *The chemistry of weathering* (pp. 19-34). Springer  
866 Netherlands.

867 Gangloff, S., Stille, P., Pierret, M. C., Weber, T., & Chabaux, F. (2014). Characterization and  
868 evolution of dissolved organic matter in acidic forest soil and its impact on the  
869 mobility of major and trace elements (case of the Strengbach watershed).  
870 *Geochimica et Cosmochimica Acta*, 130, 21-41.

871 Gérard, F. (1996). *Modélisation géochimique thermodynamique et cinétique avec prise en*  
872 *compte des phénomènes de transport de masse en milieu poreux saturé* (Doctoral  
873 dissertation).

874 Gérard, F., Clement, A., & Fritz, B. (1998). Numerical validation of a Eulerian hydrochemical  
875 code using a 1D multisolute mass transport system involving heterogeneous  
876 kinetically controlled reactions. *Journal of contaminant hydrology*, 30(3), 201-216.

877 Goddérés, Y., François, L. M., Probst, A., Schott, J., Moncoulon, D., Labat, D., & Viville, D.  
878 (2006). Modelling weathering processes at the catchment scale: The WITCH  
879 numerical model. *Geochimica et Cosmochimica Acta*, 70(5), 1128-1147.

880 Godd ris, Y., Roelandt, C., Schott, J., Pierret, M. C., & Fran ois, L. M. (2009). Towards an  
881 integrated model of weathering, climate, and biospheric processes. *Reviews in*  
882 *Mineralogy and Geochemistry*, 70(1), 411-434.

883 Godd ris, Y., & Brantley, S. L. (2013). Earthcasting the future Critical Zone. *Elementa*, 1.  
884

885 Godsey, S. E., Kirchner, J. W., & Clow, D. W. (2009). Concentration–discharge relationships  
886 reflect chemostatic characteristics of US catchments. *Hydrological Processes*, 23(13),  
887 1844-1864.

888 Hinkle, M. E. (1994). Environmental conditions affecting concentrations of He, CO<sub>2</sub>, O<sub>2</sub> and  
889 N<sub>2</sub> in soil gases. *Applied Geochemistry*, 9(1), 53-63.

890 Knight, D. H., Yavitt, J. B., & Joyce, G. D. (1991). Water and nitrogen outflow from lodgepole  
891 pine forest after two levels of tree mortality. *Forest Ecology and Management*, 46(3-  
892 4), 215-225.

893 Lasaga, A. C., Soler, J. M., Ganor, J., Burch, T. E., & Nagy, K. L. (1994). Chemical weathering  
894 rate laws and global geochemical cycles. *Geochimica et Cosmochimica Acta*, 58(10),  
895 2361-2386.

896 Lebedeva, M. I., Fletcher, R. C., & Brantley, S. L. (2010). A mathematical model for steady-  
897 state regolith production at constant erosion rate. *Earth Surface Processes and*  
898 *Landforms*, 35(5), 508-524.

899 Li, D. D., Jacobson, A. D., & McInerney, D. J. (2014). A reactive-transport model for examining  
900 tectonic and climatic controls on chemical weathering and atmospheric CO<sub>2</sub>  
901 consumption in granitic regolith. *Chemical Geology*, 365, 30-42.

902 Lovett, G. M., Christenson, L. M., Groffman, P. M., Jones, C. G., Hart, J. E., & Mitchell, M. J.  
903 (2002). Insect Defoliation and Nitrogen Cycling in Forests Laboratory, plot, and  
904 watershed studies indicate that most of the nitrogen released from forest foliage as a



905 result of defoliation by insects is redistributed within the ecosystem, whereas only a  
906 small fraction of nitrogen is lost by leaching. *BioScience*, 52(4), 335-341.

907 Lucas, Y., Schmitt, A. D., Chabaux, F., Clément, A., Fritz, B., Elsass, P., & Durand, S. (2010).  
908 Geochemical tracing and hydrogeochemical modelling of water–rock interactions  
909 during salinization of alluvial groundwater (Upper Rhine Valley, France). *Applied*  
910 *Geochemistry*, 25(11), 1644-1663.

911 Lucas, Y., Chabaux, F., Schaffhauser, T., Fritz, B., Ambroise, B., Ackerer, J., & Clément, A.  
912 (2017). Hydrogeochemical modeling (KIRMAT) of spring and deep borehole water  
913 compositions in the small granitic Ringelbach catchment (Vosges Mountains, France).  
914 *Applied Geochemistry*, 87, 1-21.

915 Maher, K., Steefel, C. I., White, A. F., & Stonestrom, D. A. (2009). The role of reaction affinity  
916 and secondary minerals in regulating chemical weathering rates at the Santa Cruz Soil  
917 Chronosequence, California. *Geochimica et Cosmochimica Acta*, 73(10), 2804-2831.

918 Maher, K. (2010). The dependence of chemical weathering rates on fluid residence time.  
919 *Earth and Planetary Science Letters*, 294(1), 101-110.

920 Maher, K. (2011). The role of fluid residence time and topographic scales in determining  
921 chemical fluxes from landscapes. *Earth and Planetary Science Letters*, 312(1), 48-58.

922 Marty, N. C., Fritz, B., Clément, A., & Michau, N. (2010). Modelling the long term alteration  
923 of the engineered bentonite barrier in an underground radioactive waste repository.  
924 *Applied Clay Science*, 47(1), 82-90.

925 Murphy, W. M., & Helgeson, H. C. (1987). Thermodynamic and kinetic constraints on  
926 reaction rates among minerals and aqueous solutions. III. Activated complexes and  
927 the pH-dependence of the rates of feldspar, pyroxene, wollastonite, and olivine  
928 hydrolysis. *Geochimica et Cosmochimica Acta*, 51(12), 3137-3153.

929 Ngo, V. V., Delalande, M., Clément, A., Michau, N., & Fritz, B. (2014). Coupled transport-  
930 reaction modeling of the long-term interaction between iron, bentonite and Callovo-  
931 Oxfordian claystone in radioactive waste confinement systems. *Applied Clay Science*,  
932 *101*, 430-443.

933 Pierret, M. C., Stille, P., Prunier, J., Viville, D., & Chabaux, F. (2014). Chemical and U–Sr  
934 isotopic variations in stream and source waters of the Strengbach watershed (Vosges  
935 mountains, France). *Hydrology and Earth System Sciences*, *18*(10), 3969-3985.

936 Probst, A., Dambrine, E., Viville, D., & Fritz, B. (1990). Influence of acid atmospheric inputs on  
937 surface water chemistry and mineral fluxes in a declining spruce stand within a small  
938 granitic catchment (Vosges massif, France). *Journal of Hydrology*, *116*(1-4), 101-124.

939 Prunier, J. (2008). *Etude du fonctionnement d'un écosystème forestier en climat tempéré, par*  
940 *l'apport de la géochimie élémentaire et isotopique (Sr, U-Th-Ra): Cas du bassin*  
941 *versant du Strengbach (Vosges, France)* (Doctoral dissertation, Strasbourg 1).

942 Prunier, J., Chabaux, F., Stille, P., Gangloff, S., Pierret, M. C., Viville, D., & Aubert, A. (2015).  
943 Geochemical and isotopic (Sr, U) monitoring of soil solutions from the Strengbach  
944 catchment (Vosges mountains, France): Evidence for recent weathering evolution.  
945 *Chemical Geology*, *417*, 289-305.

946 Schaffhauser, T. (2013). *Traçage et modélisation des processus d'altération à l'échelle d'un*  
947 *petit bassin versant, le Ringelbach (Vosges, France)* (Doctoral dissertation,  
948 Strasbourg).

949 Schaffhauser, T., Chabaux, F., Ambroise, B., Lucas, Y., Stille, P., Reuschlé, T., ... & Fritz, B.  
950 (2014). Geochemical and isotopic (U, Sr) tracing of water pathways in the granitic  
951 Ringelbach catchment (Vosges Mountains, France). *Chemical Geology*, *374*, 117-127.

952 Sirocko, F., Knapp, H., Dreher, F., Förster, M. W., Albert, J., Brunck, H., ... & Röhner, M.  
953 (2016). The ELSA-Vegetation-Stack: Reconstruction of Landscape Evolution Zones  
954 (LEZ) from laminated Eifel maar sediments of the last 60,000 years. *Global and*  
955 *Planetary Change*, 142, 108-135.

956 Stille, P., Pierret, M. C., Steinmann, M., Chabaux, F., Boutin, R., Aubert, D., ... & Morvan, G.  
957 (2009). Impact of atmospheric deposition, biogeochemical cycling and water–mineral  
958 interaction on REE fractionation in acidic surface soils and soil water (the Strengbach  
959 case). *Chemical Geology*, 264(1), 173-186.

960 Tardy, Y., & Fritz, B. (1981). An ideal solid solution model for calculating solubility of clay  
961 minerals. *Clay minerals*, 16(3), 361-373.

962 Thompson, S. E., Basu, N. B., Lascrain, J., Aubeneau, A., & Rao, P. S. C. (2011). Relative  
963 dominance of hydrologic versus biogeochemical factors on solute export across  
964 impact gradients. *Water Resources Research*, 47(10).

965 Viville, D., Chabaux, F., Stille, P., Pierret, M. C., & Gangloff, S. (2012). Erosion and weathering  
966 fluxes in granitic basins: the example of the Strengbach catchment (Vosges massif,  
967 eastern France). *Catena*, 92, 122-129.

968 Viville D., Ladouche B., Bariac T. (2006). Isotope hydrological study of mean transit time in  
969 the granitic Strengbach catchment (Vosges Massif, France). *Hydrol. Process.* 20, 1737-  
970 1751. doi: 10.1002/hyp.5950.

971 White, A. F., & Brantley, S. L. (2003). The effect of time on the weathering of silicate  
972 minerals: why do weathering rates differ in the laboratory and field?. *Chemical*  
973 *Geology*, 202(3), 479-506.

974 Wild, B., Daval, D., Guyot, F., Knauss, K. G., Pollet-Villard, M., & Imfeld, G. (2016). pH-  
975 dependent control of feldspar dissolution rate by altered surface layers. *Chemical*  
976 *Geology*, 442, 148-159.

977 WRB, 2006. International Union Soil Sciences Working Group WRB. 2006. World reference  
978 base for soil resources 2006. World Soil Resources Reports No. 103. FAO, Rome  
979  
980  
981

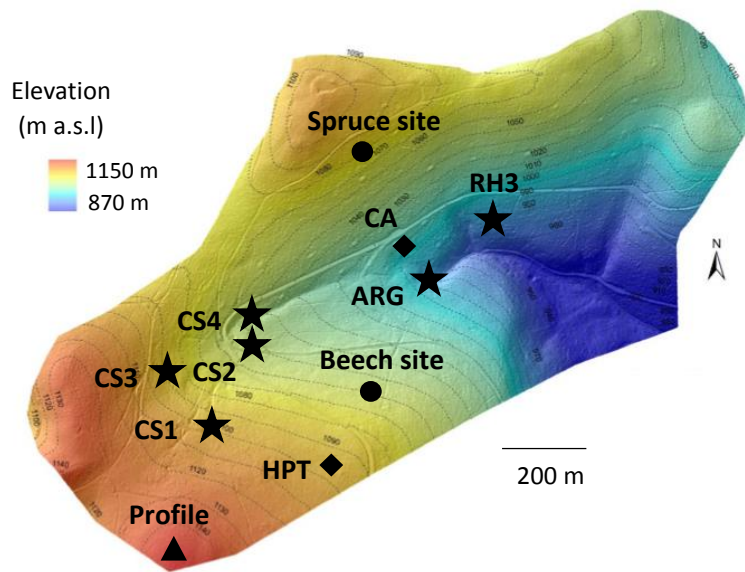


Figure 1

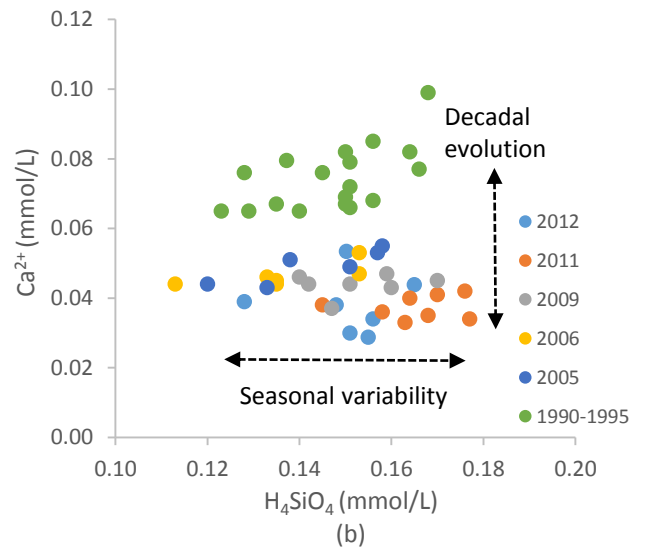
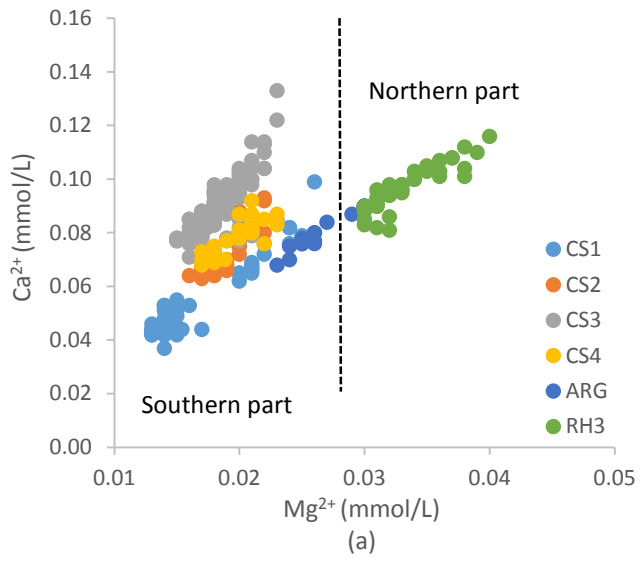


Figure 2

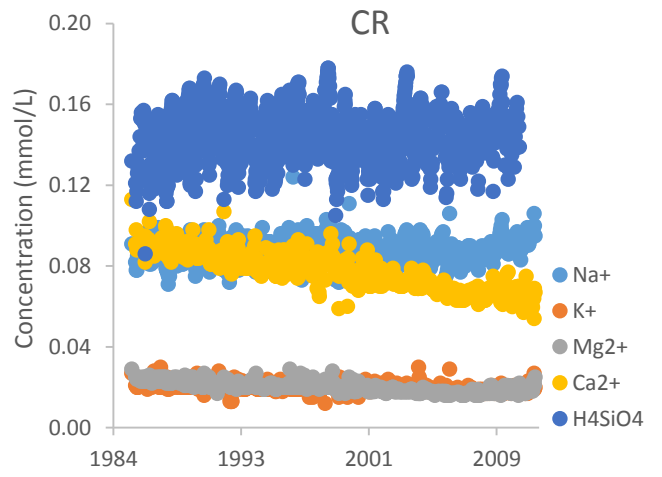
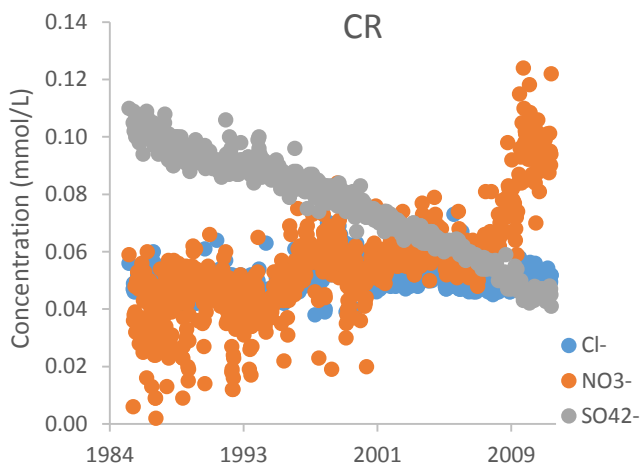


Figure 3

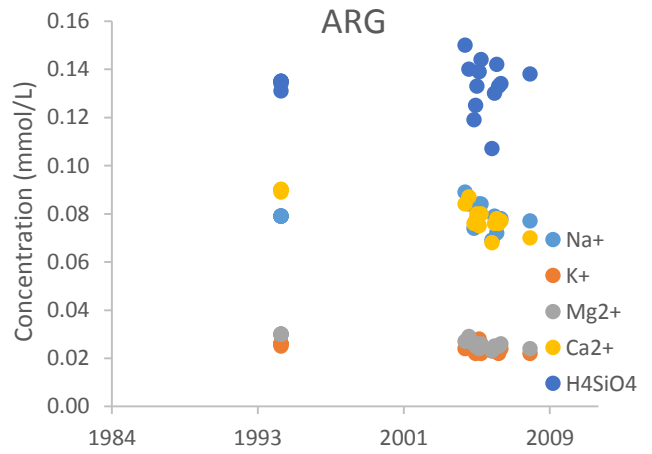
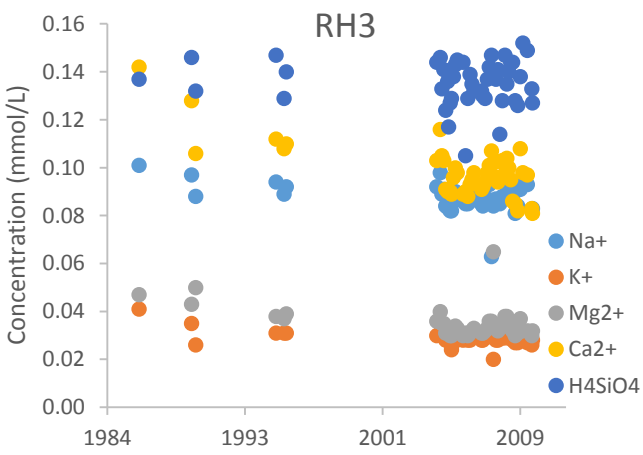
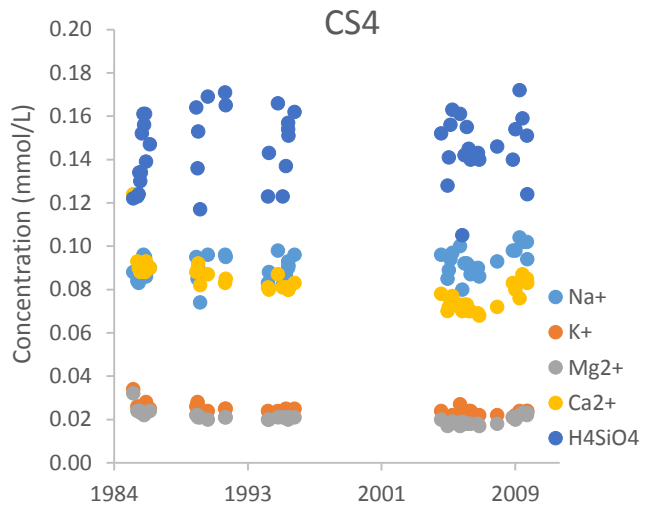
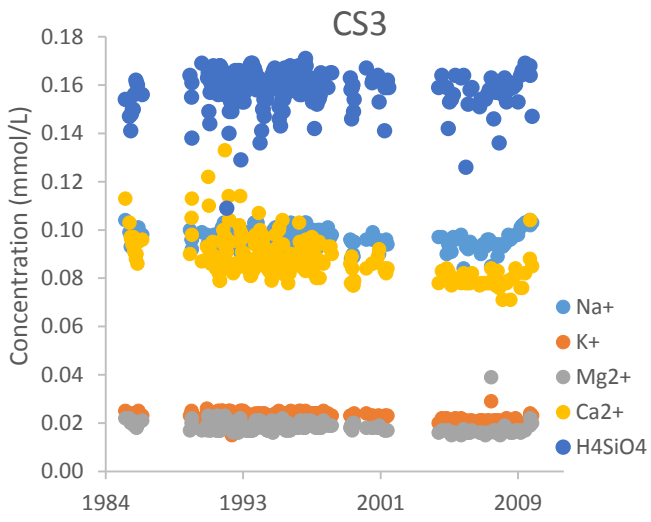
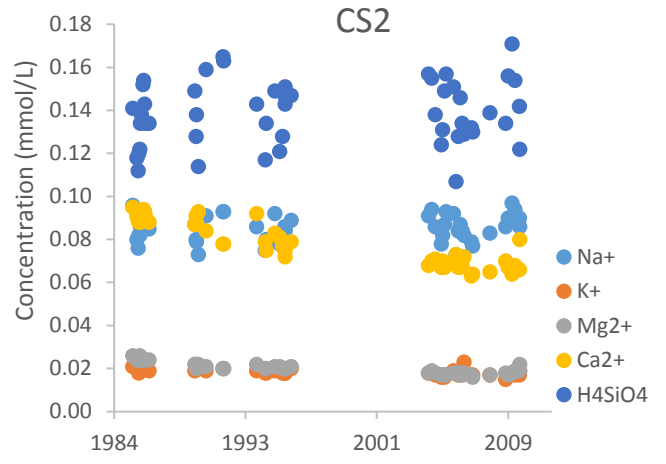
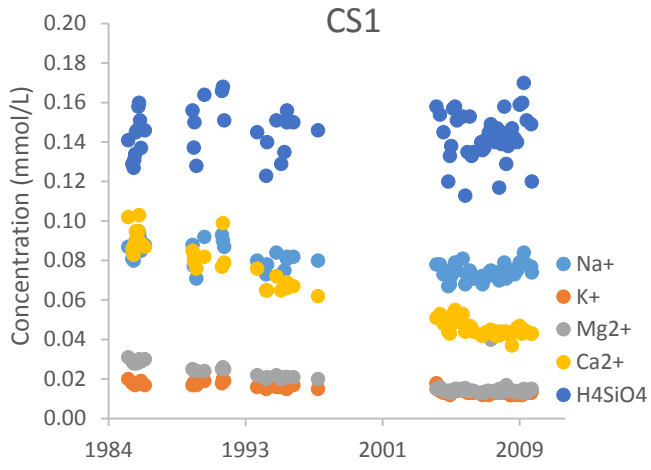


Figure 4



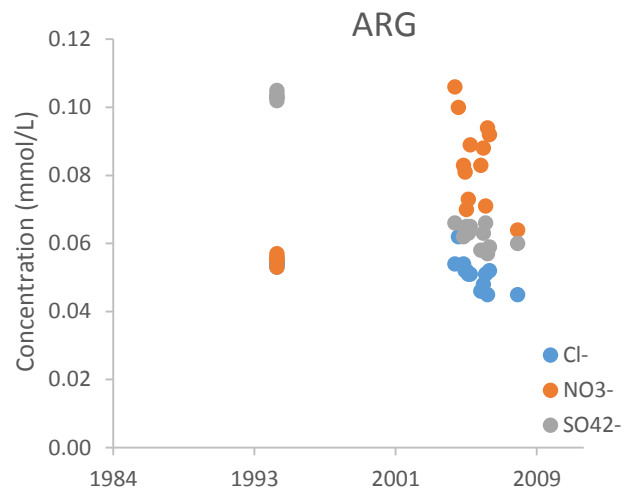
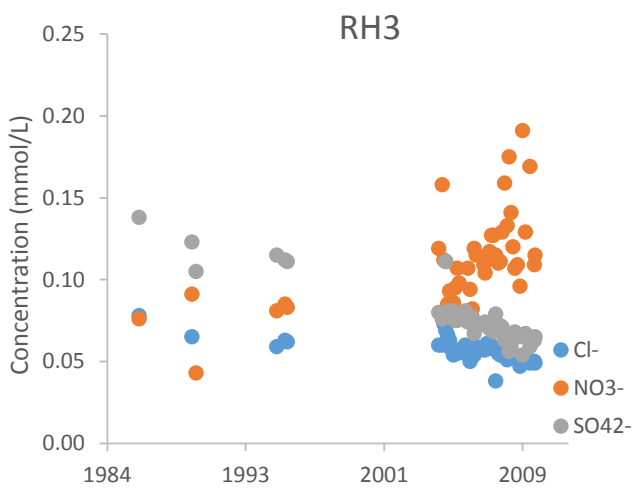
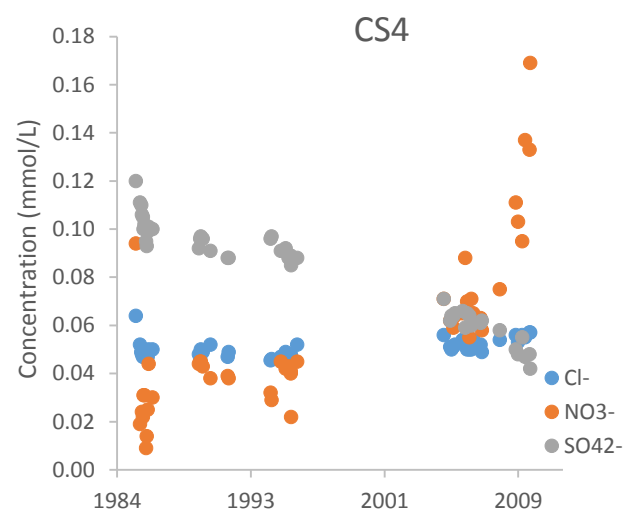
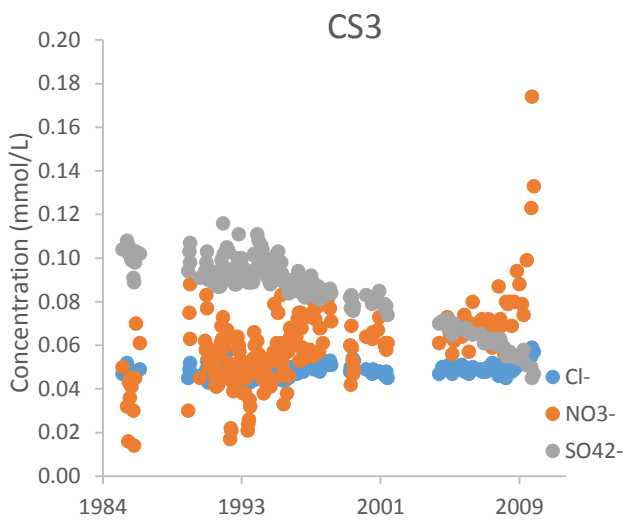
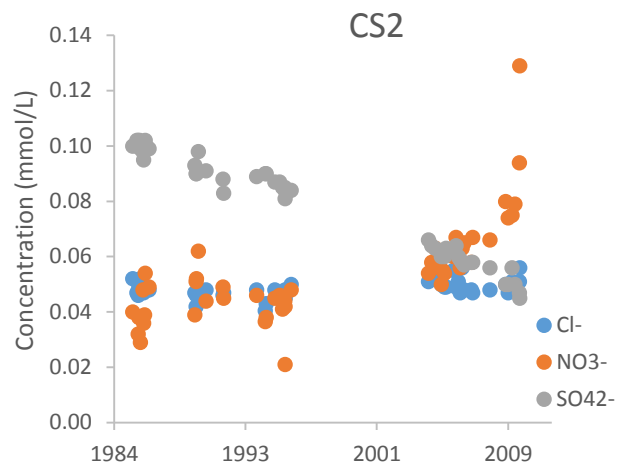
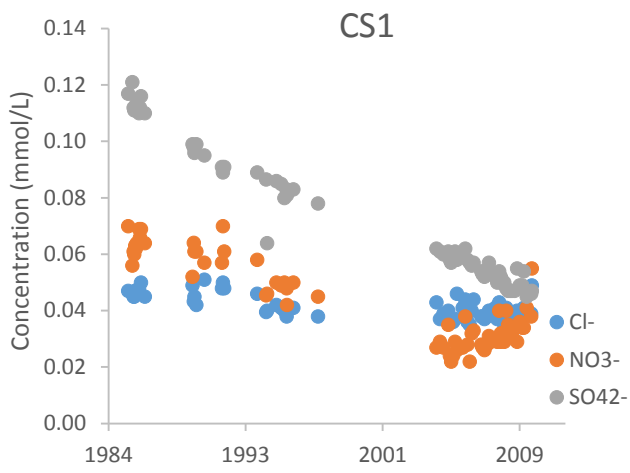


Figure 5

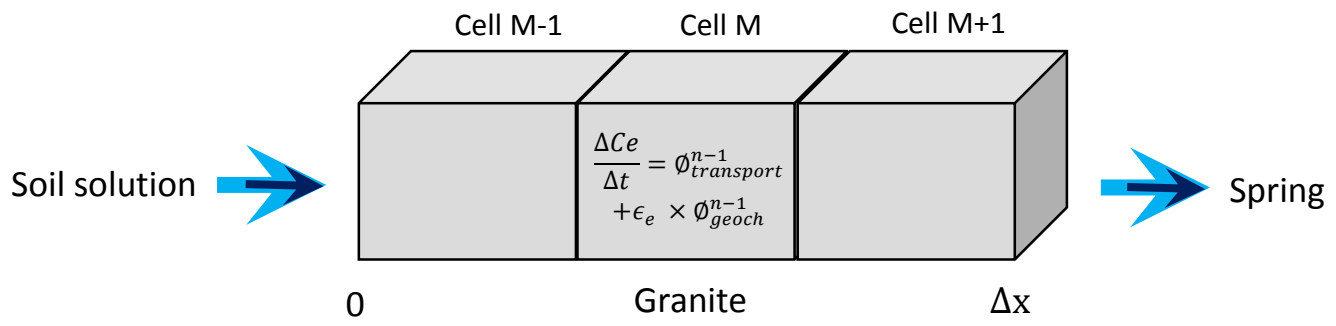


Figure 6

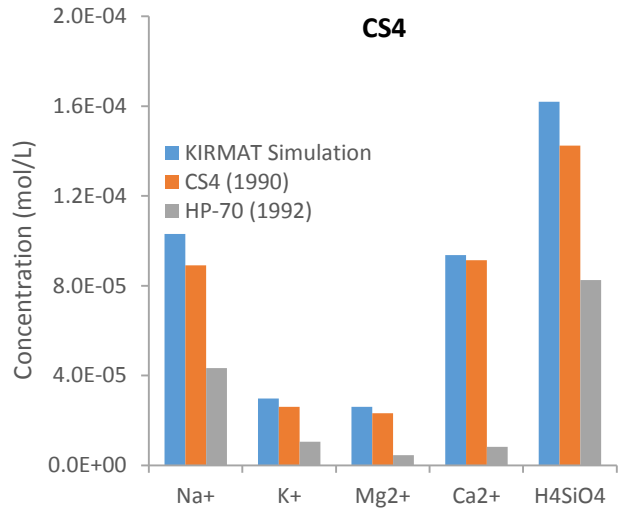
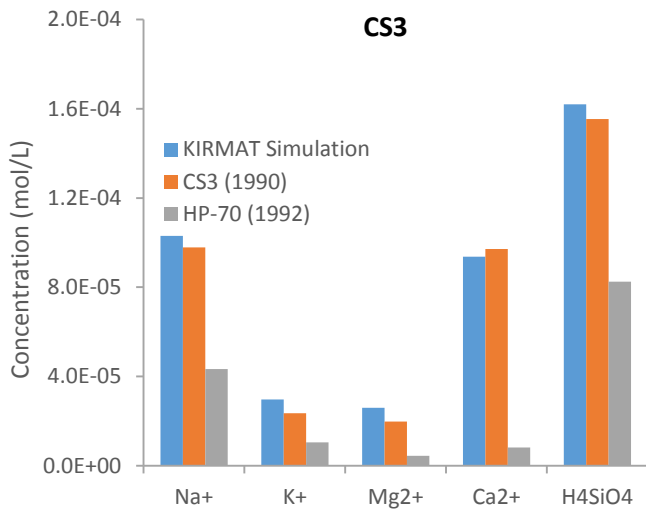
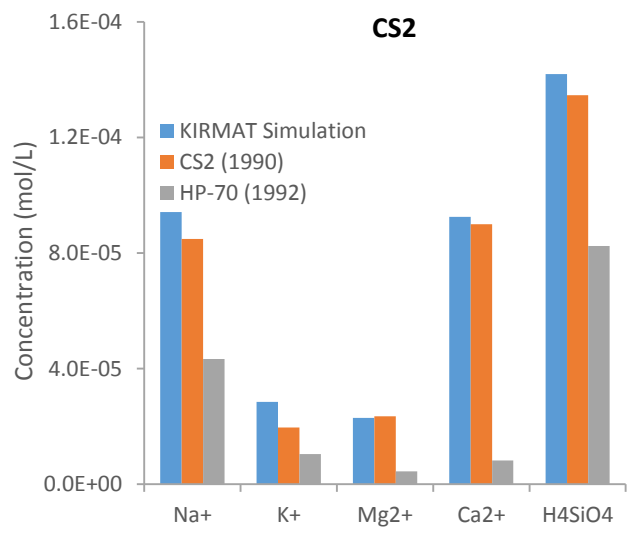
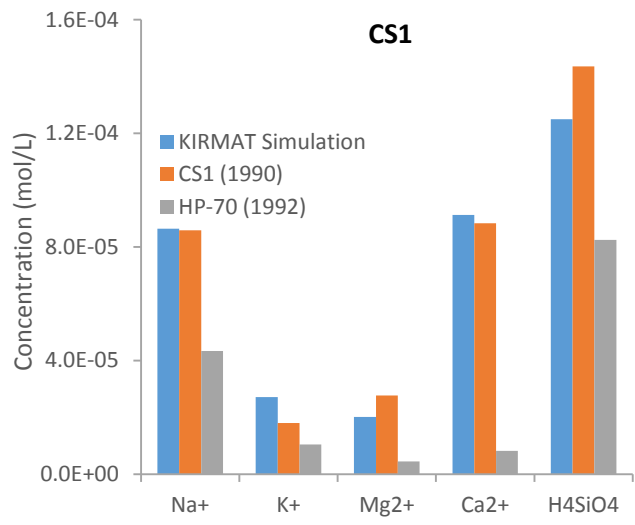


Figure 7

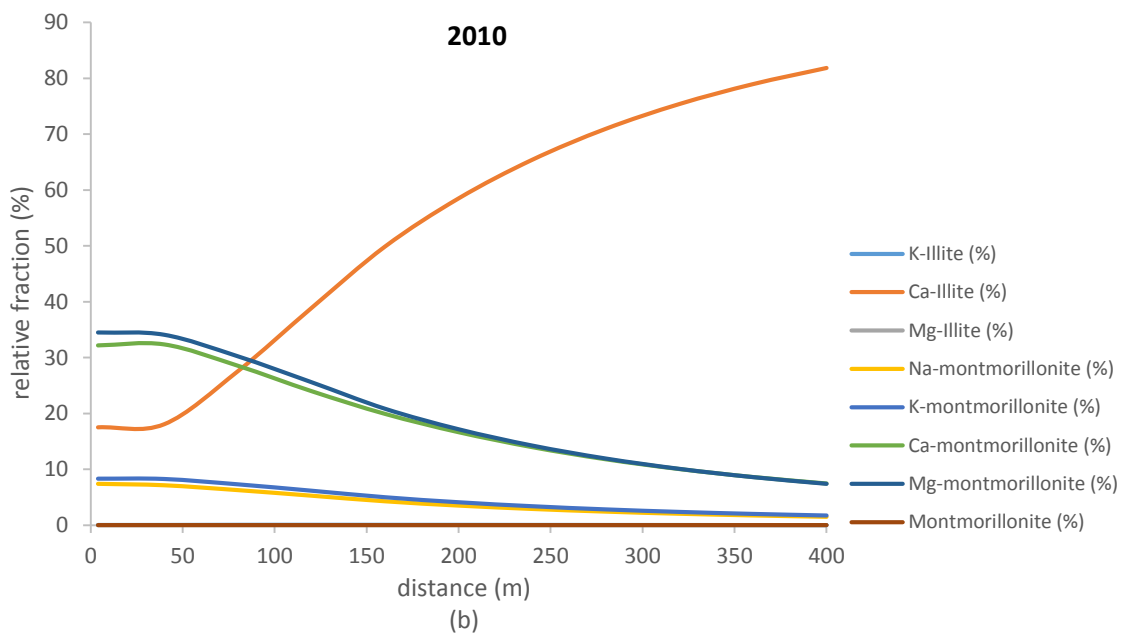
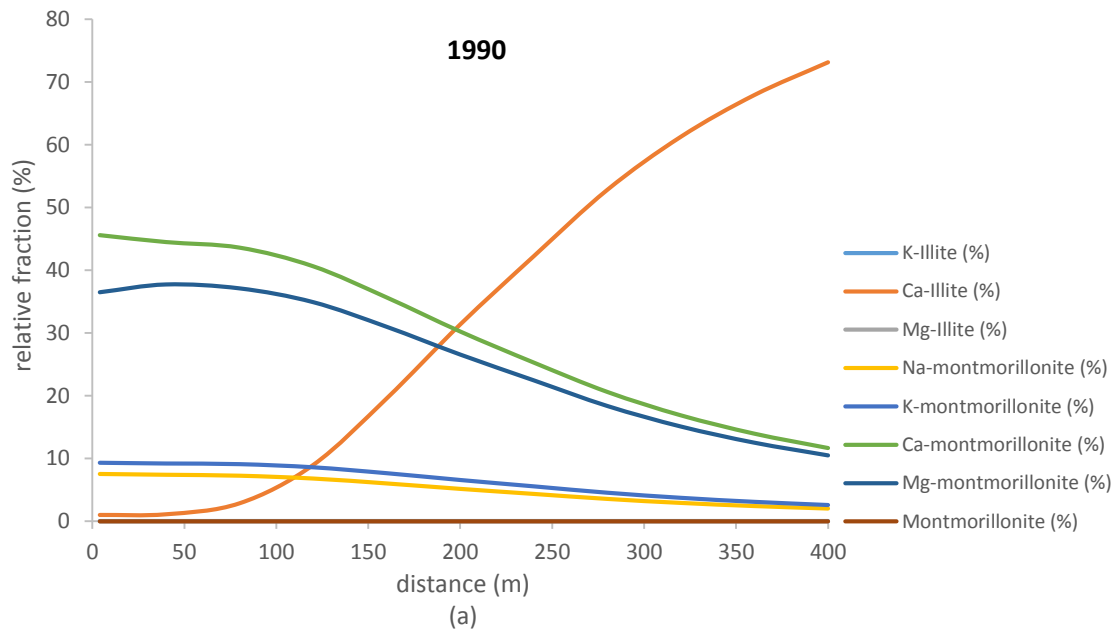


Figure 8

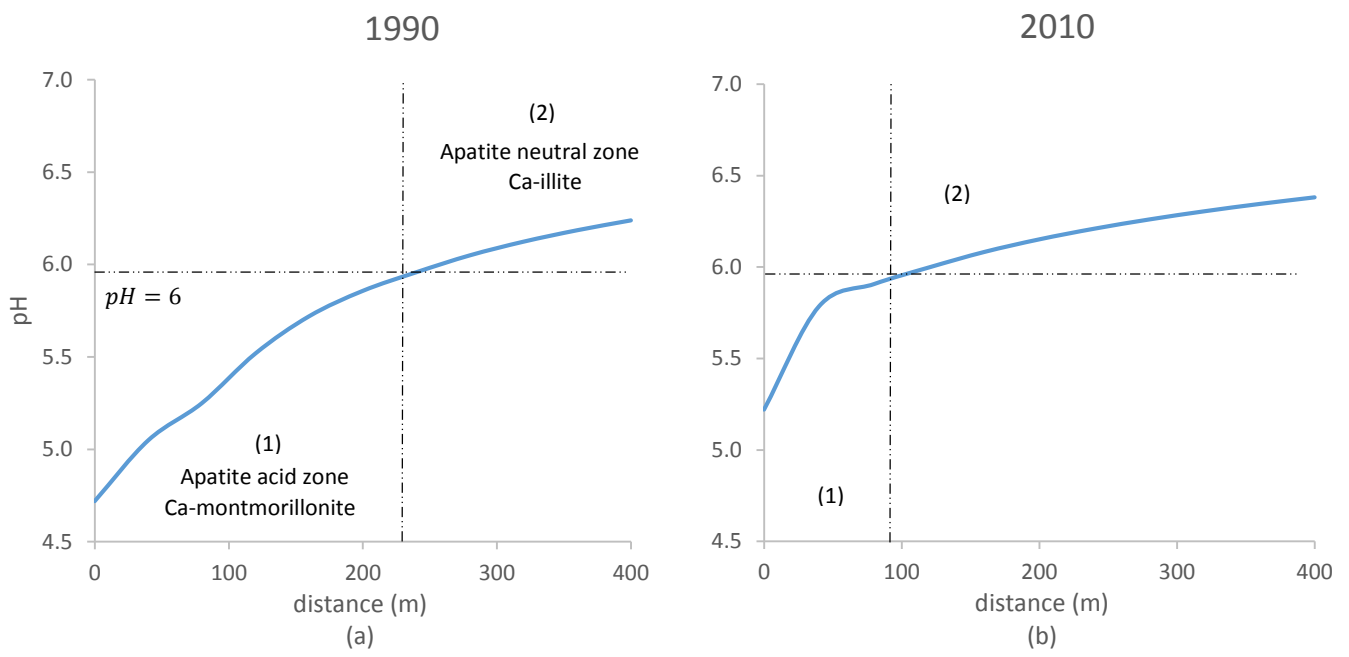


Figure 9

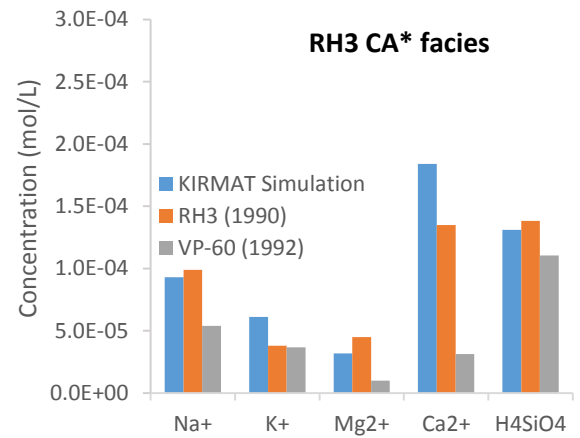
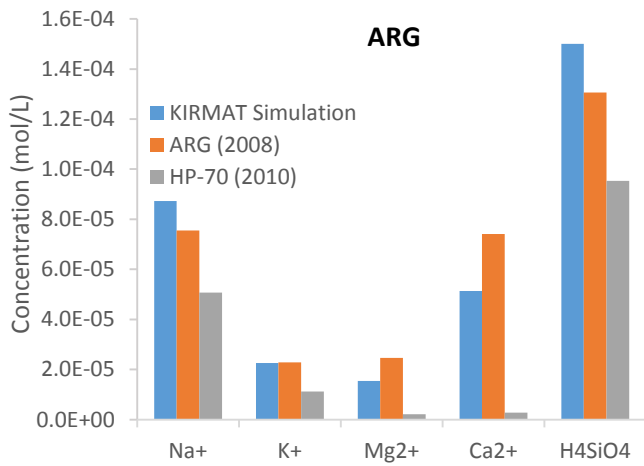
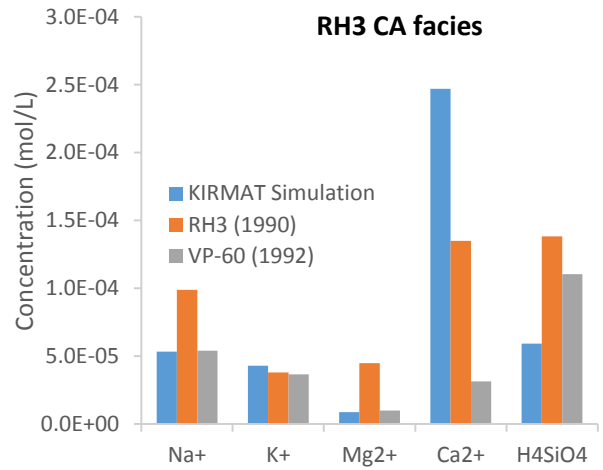
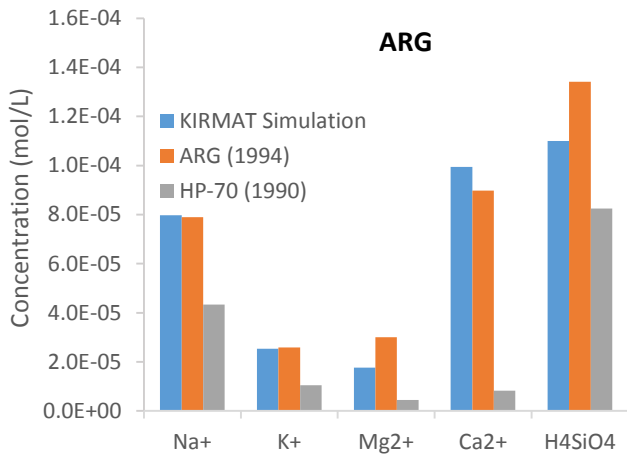


Figure 10

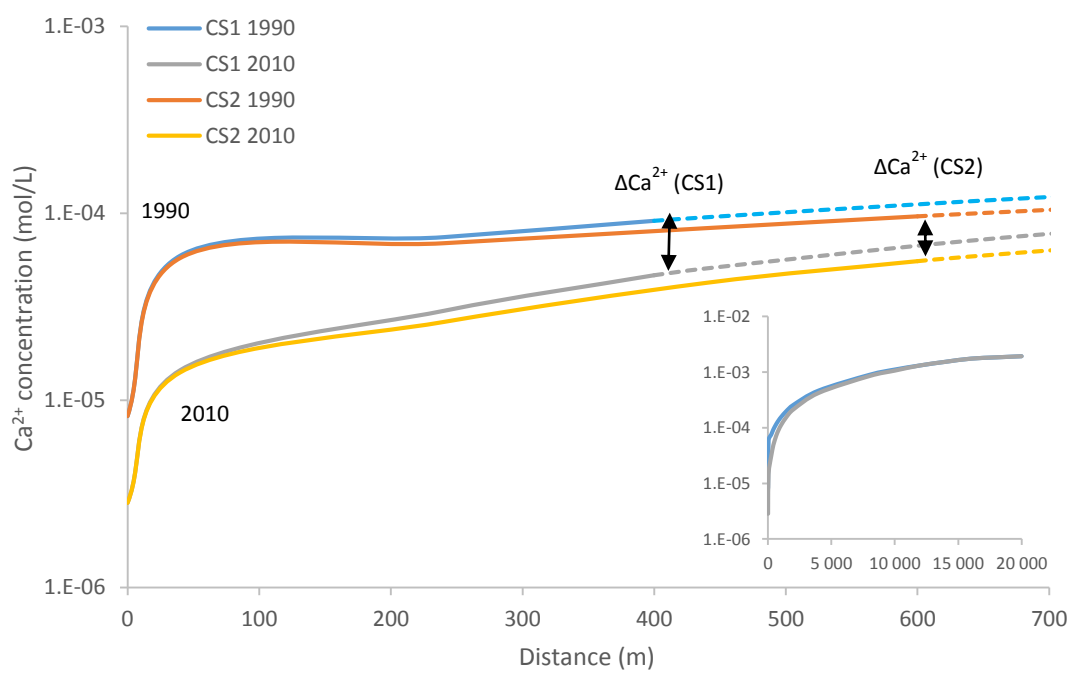


Figure 11





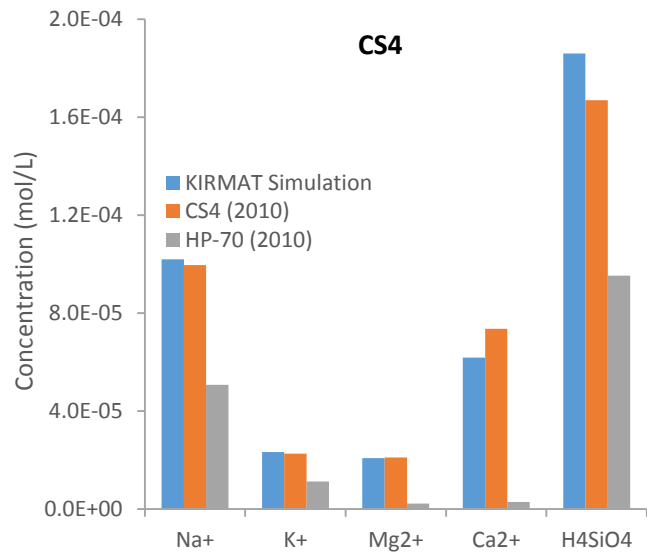
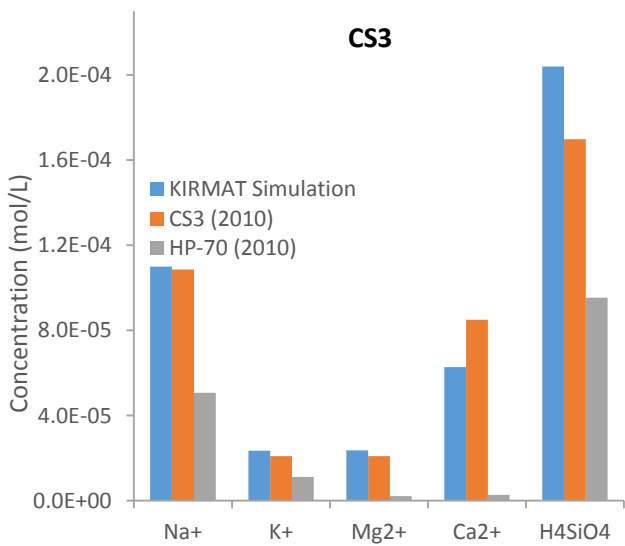
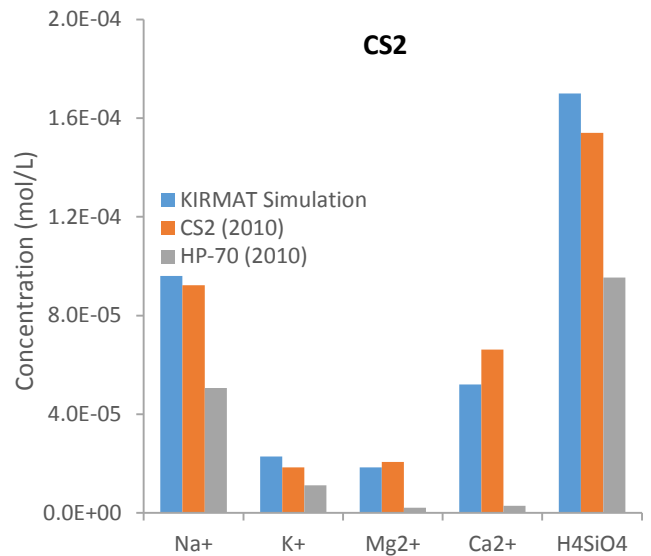
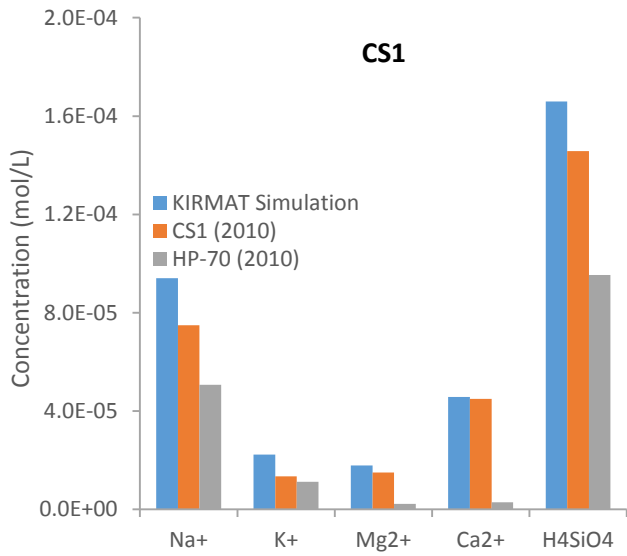


Figure 12

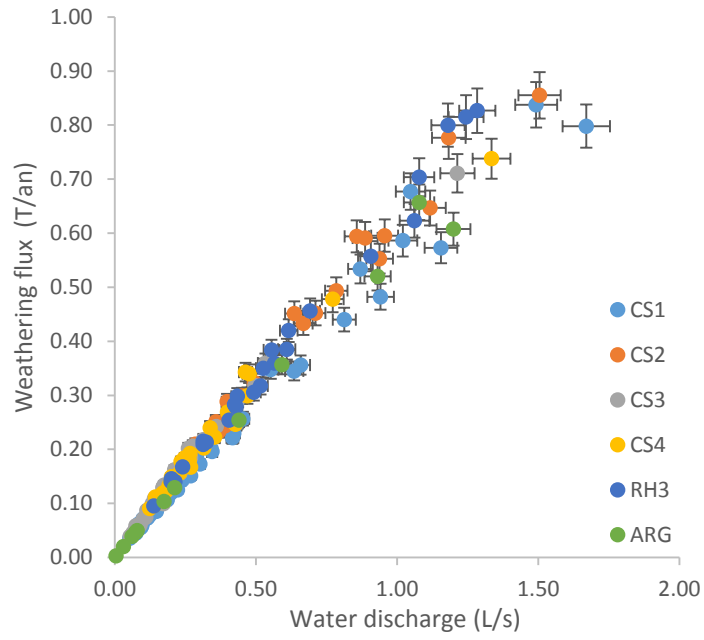


Figure 13

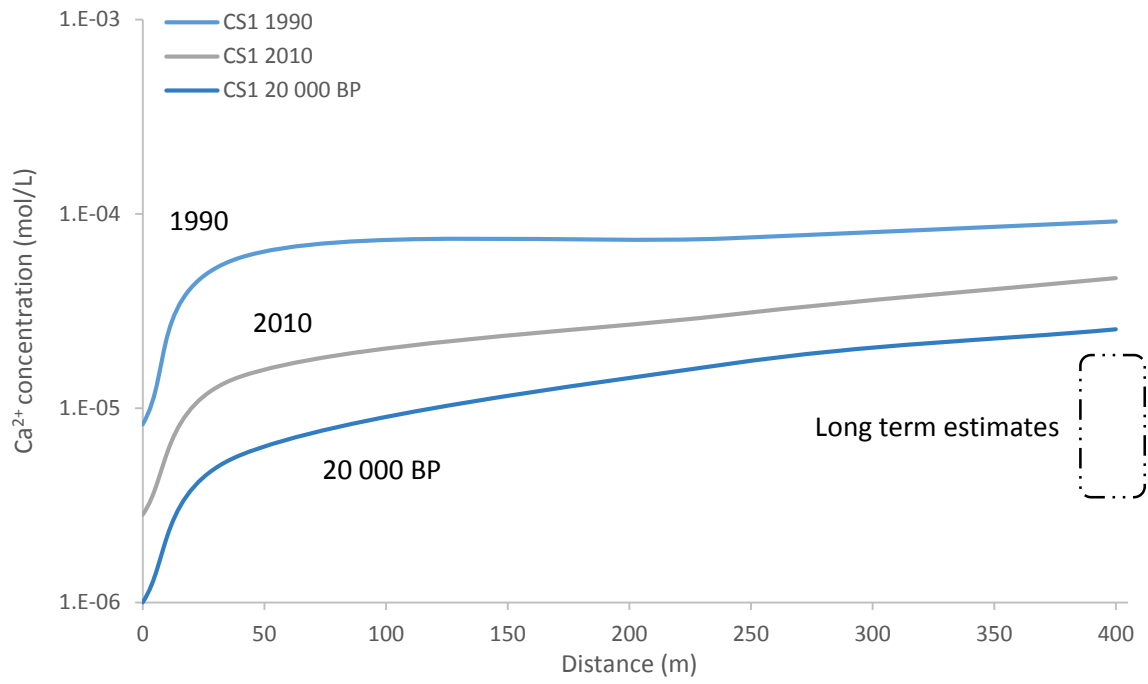


Figure 14

Mineral	Mass fraction (HPT facies) (%)	Reactive surface area (HPT facies) (m <sup>2</sup> /kg H <sub>2</sub> O)	Mass fraction (CA facies) (%)	Reactive surface area (CA facies) (m <sup>2</sup> /kg H <sub>2</sub> O)	Mass fraction (CA* facies) (%)	Reactive surface area (CA* facies) (m <sup>2</sup> /kg H <sub>2</sub> O)
Quartz	35	19.45	46	25.56	46	25.56
Albite	31	12.92	0	0	7	2.92
K-feldspar	22	5.16	5	1.17	5	1.17
Biotite	6	10.23	0	0	2	3.41
Muscovite	3	5.11	48	81.84	38	64.79
Anorthite	2	0.83	0	0	0	0
Apatite	0.5	0.02	0.3	0.004	0.3	0.004
Illite	0.5	18.75	0.7	26.26	1.7	63.77

Table 1

(T/km <sup>2</sup> /yr)	Na <sup>+</sup>	K <sup>+</sup>	Mg <sup>2+</sup>	Ca <sup>2+</sup>	H <sub>4</sub> SiO <sub>4</sub>
CS1 spring					
(F)	0.30 ± 0.06	0.10 ± 0.02	0.07 ± 0.02	0.38 ± 0.07	2.29 ± 0.45
(A)	0.08 ± 0.02	0	0.04 ± 0.01	0.24 ± 0.06	2.23 ± 0.55
(B)	0.10 ± 0.03	0.01 ± 0.004	0.05 ± 0.02	0.31 ± 0.09	2.34 ± 0.58
(C)	0.10 ± 0.03	0.07 ± 0.028	0.06 ± 0.03	0.37 ± 0.11	2.37 ± 0.59
CS2 spring					
(F)	0.34 ± 0.07	0.13 ± 0.03	0.08 ± 0.02	0.53 ± 0.10	2.26 ± 0.45
(A)	0.10 ± 0.02	0	0.05 ± 0.01	0.33 ± 0.08	2.20 ± 0.55
(B)	0.11 ± 0.03	0.02 ± 0.008	0.06 ± 0.02	0.43 ± 0.13	2.31 ± 0.57
(C)	0.12 ± 0.04	0.09 ± 0.036	0.07 ± 0.02	0.52 ± 0.16	2.34 ± 0.58
CS3 spring					
(F)	0.28 ± 0.06	0.11 ± 0.02	0.06 ± 0.01	0.45 ± 0.09	2.76 ± 0.55
(A)	0.08 ± 0.02	0	0.04 ± 0.01	0.28 ± 0.07	2.69 ± 0.67
(B)	0.09 ± 0.03	0.02 ± 0.008	0.04 ± 0.01	0.37 ± 0.11	2.83 ± 0.70
(C)	0.10 ± 0.03	0.07 ± 0.028	0.05 ± 0.02	0.44 ± 0.13	2.86 ± 0.71
CS4 spring					
(F)	0.32 ± 0.07	0.14 ± 0.03	0.07 ± 0.02	0.47 ± 0.10	2.09 ± 0.52
(A)	0.09 ± 0.02	0	0.04 ± 0.01	0.29 ± 0.07	2.03 ± 0.51
(B)	0.11 ± 0.03	0.02 ± 0.008	0.05 ± 0.02	0.38 ± 0.11	2.14 ± 0.54
(C)	0.11 ± 0.03	0.09 ± 0.036	0.06 ± 0.02	0.46 ± 0.14	2.17 ± 0.54
Regolith profile	0.22 ± 0.14	0.39 ± 0.25	0.02 ± 0.01	0.04 ± 0.02	3 ± 2

Table 2

## Electronic Annex Figures

Figure 1: concentration time evolutions of cations ( $\text{Na}^+$ ,  $\text{K}^+$ ,  $\text{Ca}^{2+}$ ,  $\text{Mg}^{2+}$ ) for the PA rainfalls collected at the summit of the Strengbach watershed from 1986 to 2010.

Figure 2: concentration time evolutions of anions and dissolved silica ( $\text{SO}_4^{2-}$ ,  $\text{NO}_3^-$ ,  $\text{Cl}^-$ ,  $\text{H}_4\text{SiO}_4$ ) for the PA rainfalls collected at the summit of the Strengbach watershed from 1986 to 2010.

Figure 3: measured pH for the soil solutions VP-60, HP-70, and for the PA rainfalls and the CR waters from 1986 to 2010.

Figure 4: concentration time evolutions of cations ( $\text{Na}^+$ ,  $\text{K}^+$ ,  $\text{Ca}^{2+}$ ,  $\text{Mg}^{2+}$ ) for the soil solution VP-60 collected at the spruce site from 1992 to 2010.

Figure 5: concentration time evolutions of cations ( $\text{Na}^+$ ,  $\text{K}^+$ ,  $\text{Ca}^{2+}$ ,  $\text{Mg}^{2+}$ ) for the soil solution HP-70 collected at the beech site from 1992 to 2010.

Figure 6: concentration time evolutions of anions and dissolved silica ( $\text{SO}_4^{2-}$ ,  $\text{NO}_3^-$ ,  $\text{Cl}^-$ ,  $\text{H}_4\text{SiO}_4$ ) for the soil solution VP-60 collected at the spruce site from 1992 to 2010.

Figure 7: concentration time evolutions of anions and dissolved silica ( $\text{SO}_4^{2-}$ ,  $\text{NO}_3^-$ ,  $\text{Cl}^-$ ,  $\text{H}_4\text{SiO}_4$ ) for the soil solution HP-70 collected at the beech site from 1992 to 2010.

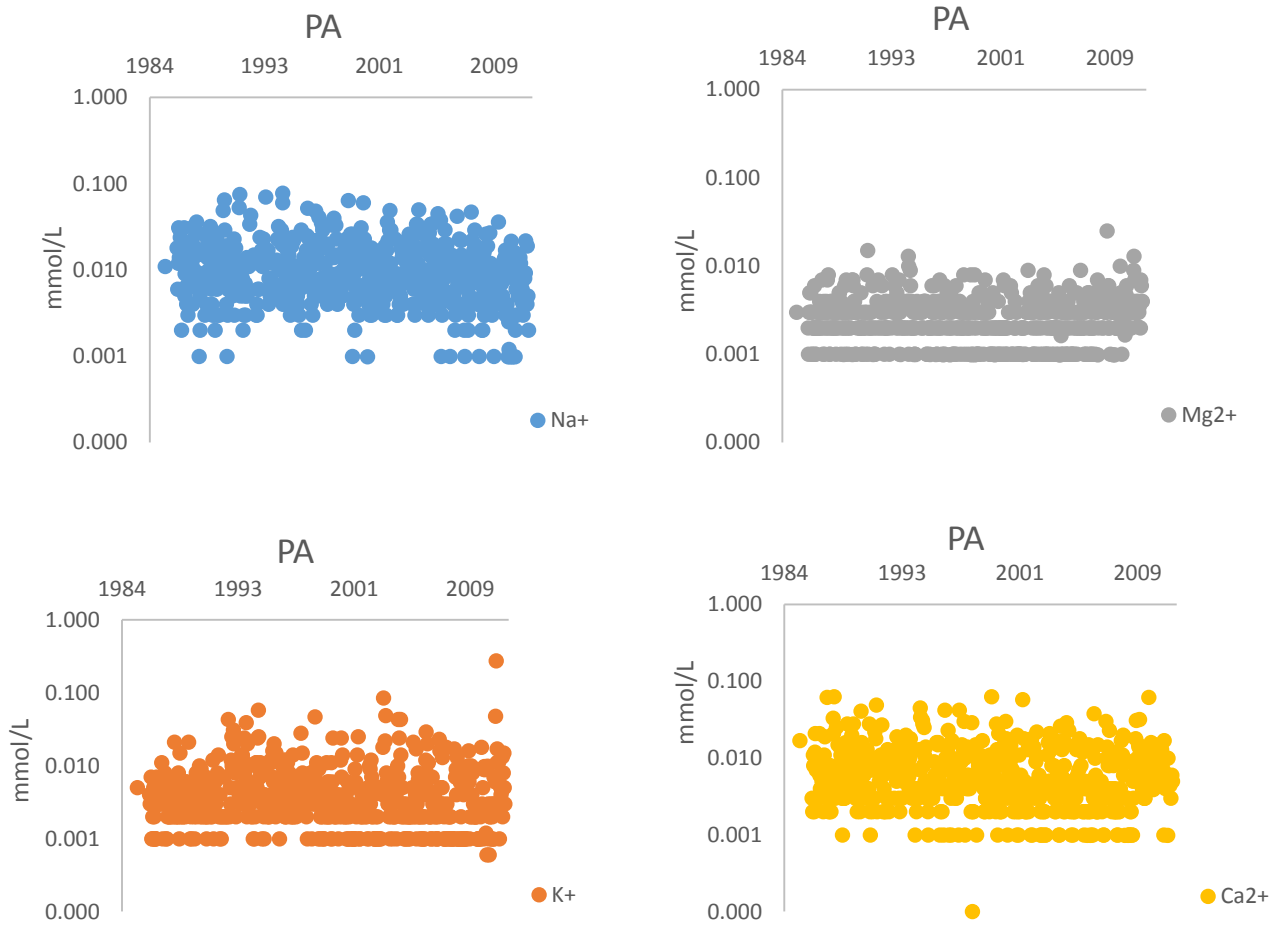


Figure 1

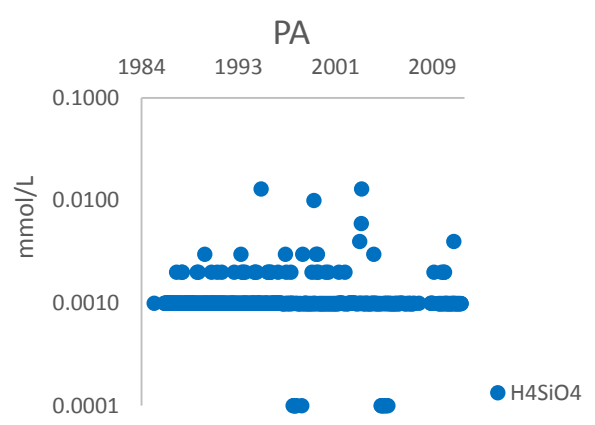
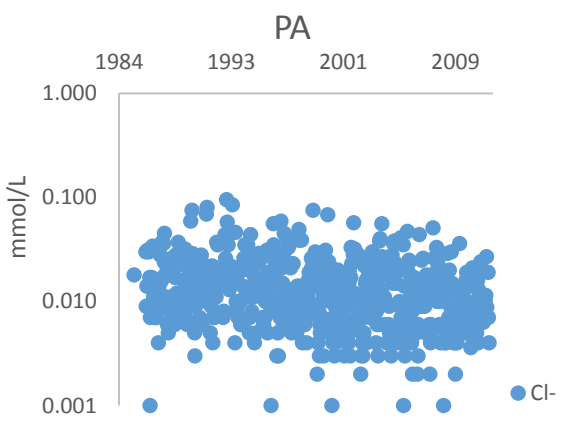
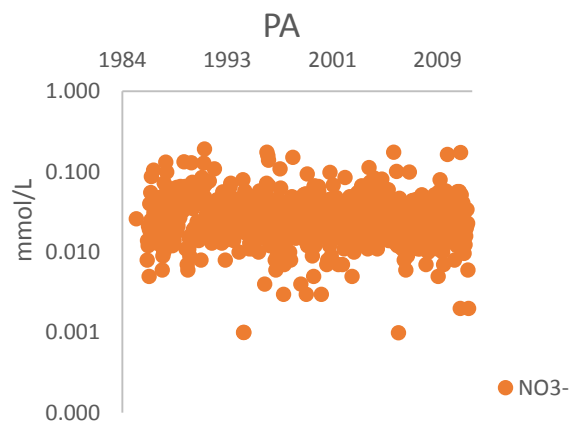
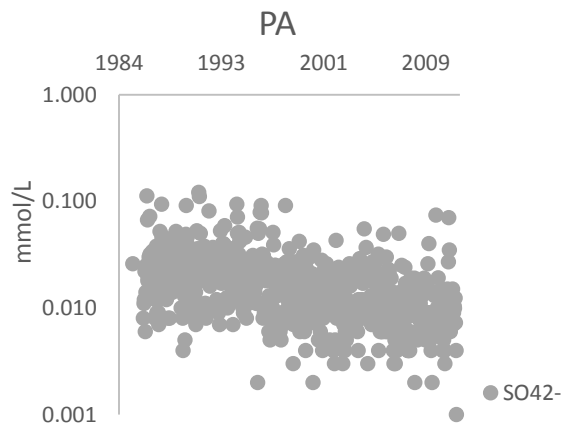


Figure 2



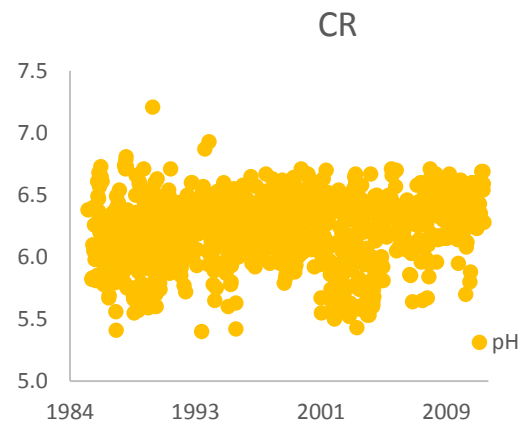
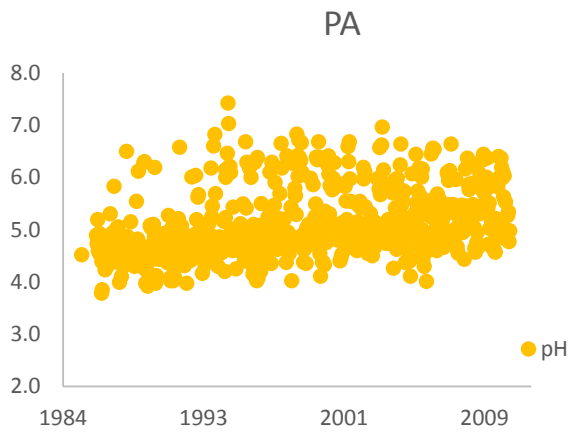
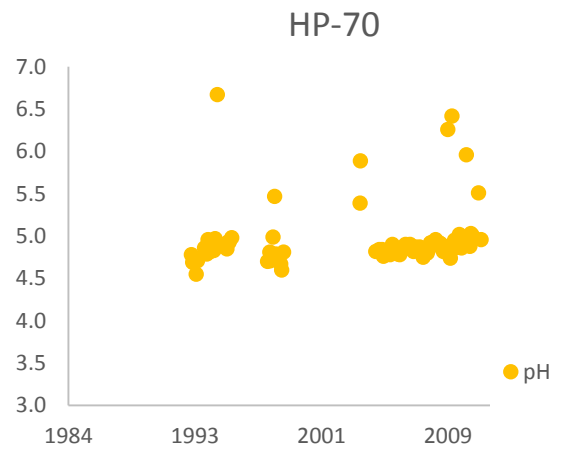
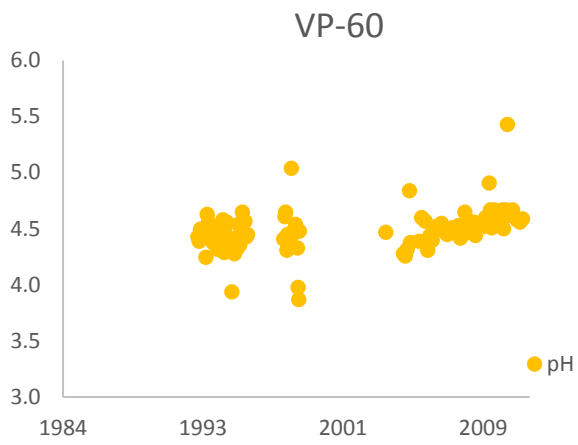


Figure 3

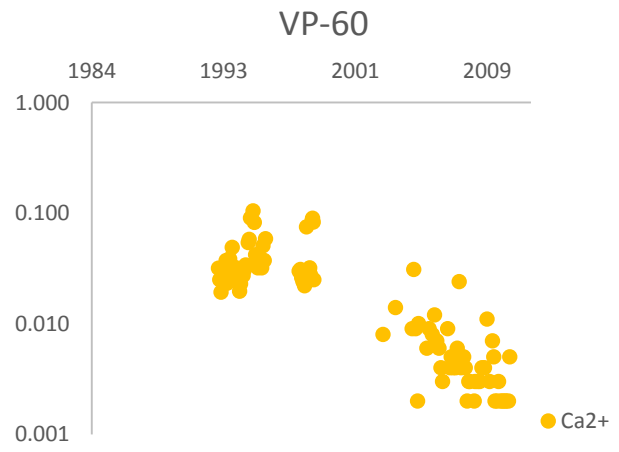
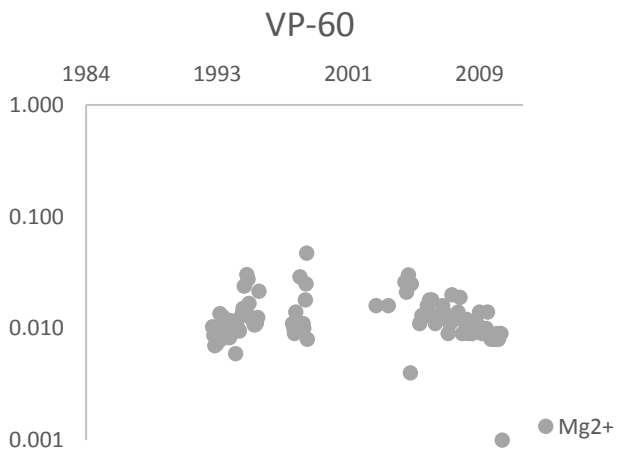
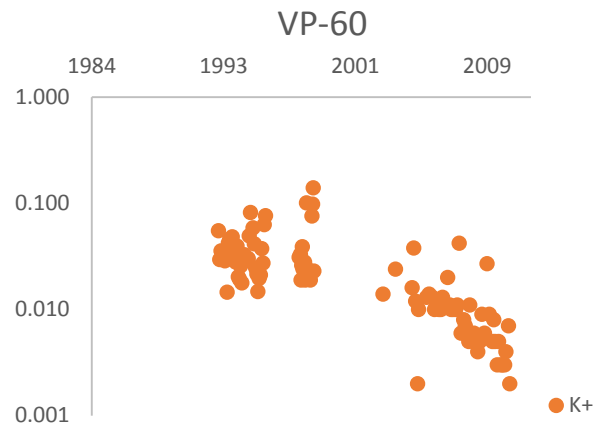
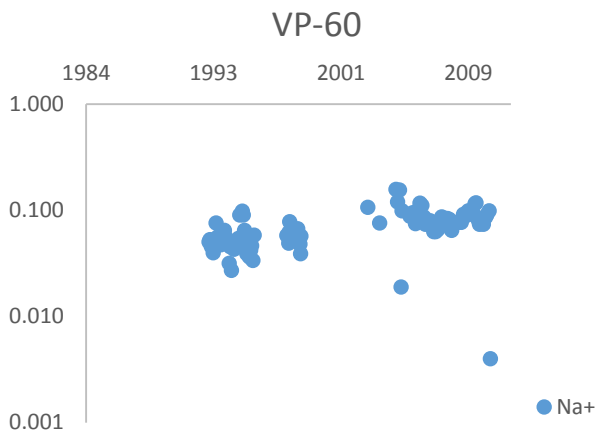


Figure 4

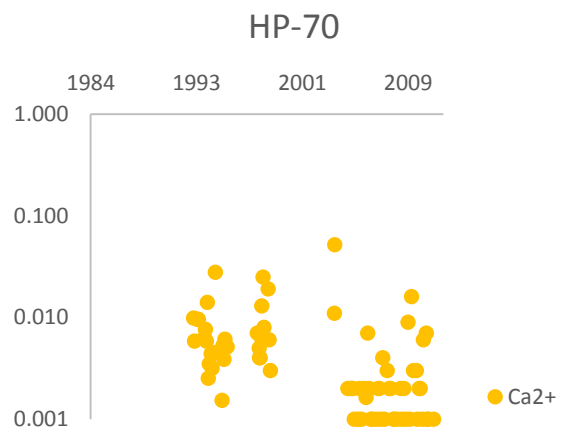
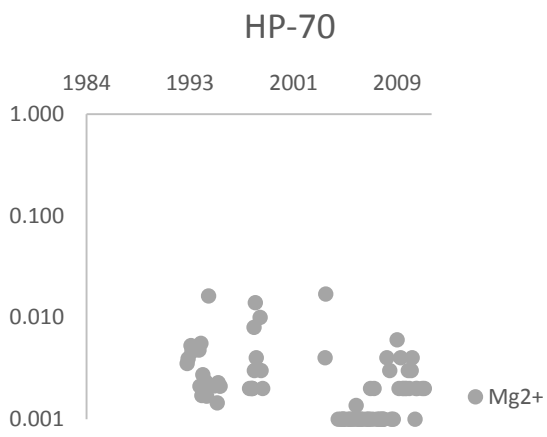
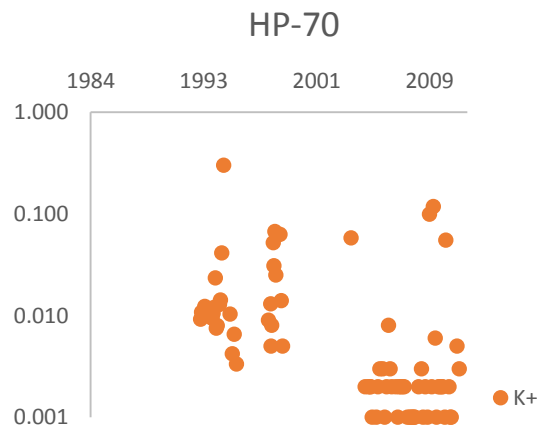
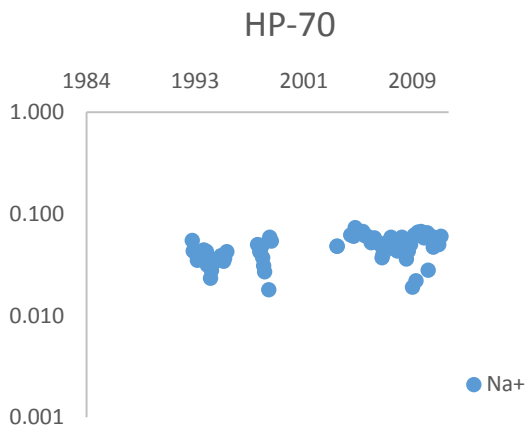


Figure 5

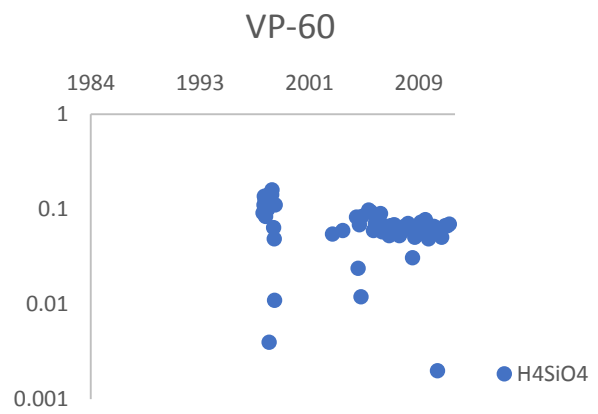
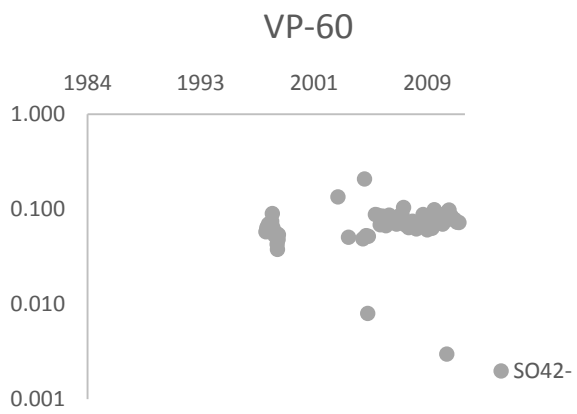
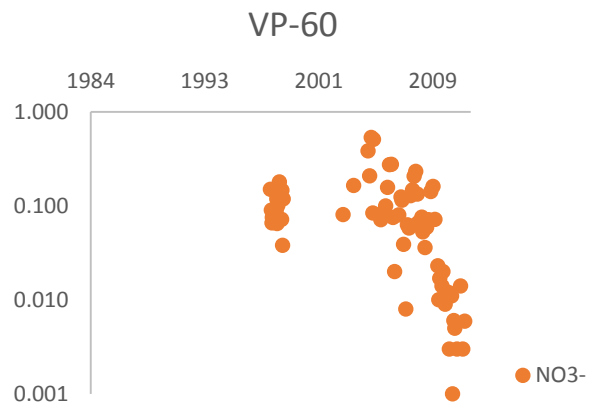
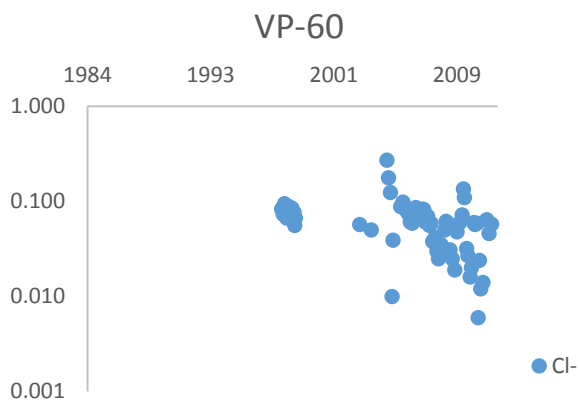


Figure 6

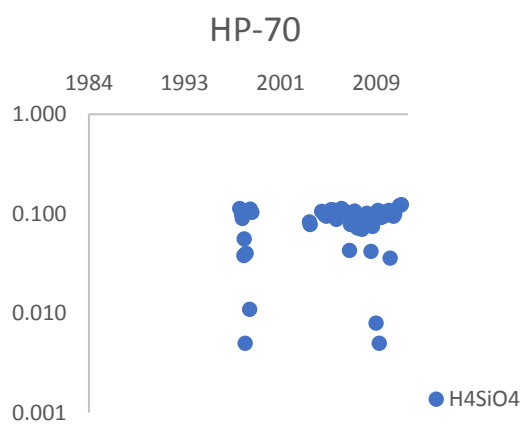
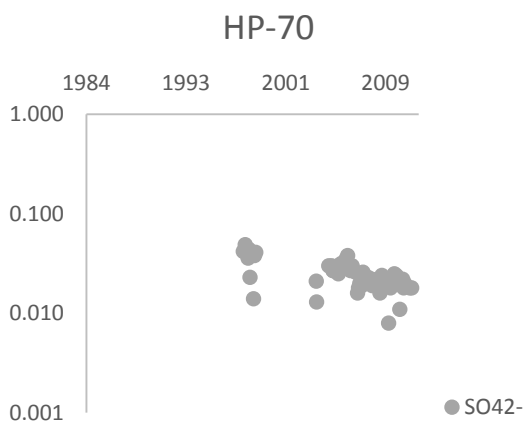
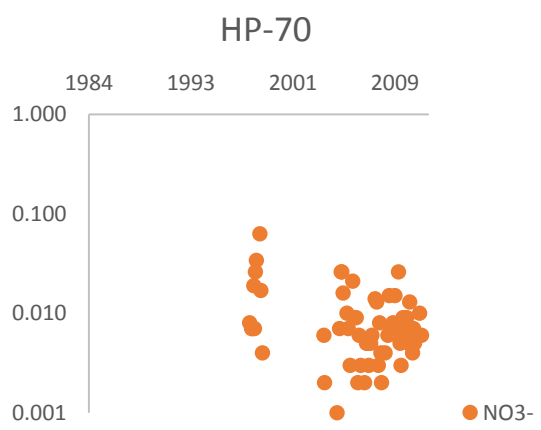
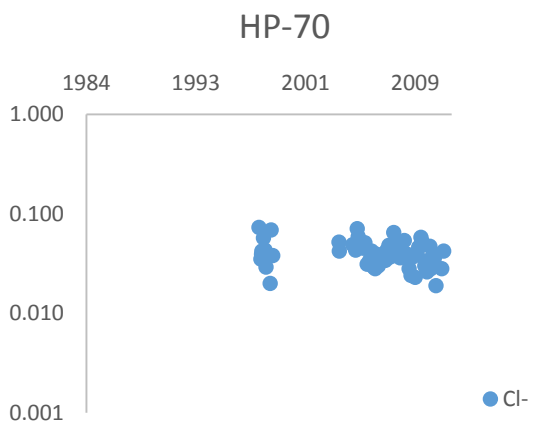


Figure 7

